

1 **The optical properties, physical properties and direct radiative**  
2 **forcing of urban columnar aerosols in the Yangtze River Delta,**  
3 **China**

4 Bingliang Zhuang<sup>1,\*</sup>, Tijian Wang<sup>1,\*\*</sup>, Jane. Liu<sup>1,2</sup>, Huizheng Che<sup>3</sup>, Yong Han<sup>1</sup>, Yu  
5 Fu<sup>4</sup>, Shu Li<sup>1</sup>, Min Xie<sup>1</sup>, Mengmeng Li<sup>1</sup>, Pulong Chen<sup>1</sup>, Huimin Chen<sup>1</sup>, Xiu-qun Yang<sup>1</sup>,

6 Jianning Sun<sup>1</sup>

7 <sup>1</sup> School of Atmospheric Sciences, CMA-NJU Joint Laboratory for Climate Prediction Studies, Jiangsu  
8 Collaborative Innovation Center for Climate Change, Nanjing University, Nanjing 210023, China

9 <sup>2</sup> Department of Geography and Planning, University of Toronto, Toronto, M5S 3G3, Canada

10 <sup>3</sup> Key Laboratory of Atmospheric Chemistry (LAC), Chinese Academy of Meteorological Sciences (CAMS),  
11 CMA, Beijing, 100081, China

12 <sup>4</sup> Dalian Weather Modification Office, Dalian, 116001, China

13 \* Corresponding author, E-mail: [blzhuang@nju.edu.cn](mailto:blzhuang@nju.edu.cn); Tel.: +862589681156; Fax: +862589683797

14 \*\* Corresponding author, E-mail: [tjwang@nju.edu.cn](mailto:tjwang@nju.edu.cn); Tel.: +862589683797; Fax: +862589683797

15

16 **Abstract:** The optical and physical properties as well as the direct radiative forcings (DRF) of  
17 fractionated aerosols in the urban area of the western Yangtze River Delta (YRD) are investigated with  
18 measurements from a Cimel sun photometer combined with a radiation transfer model. Ground-based  
19 observations of aerosols have much higher temporal resolutions than satellite retrievals. An initial  
20 analysis reveals the characteristics of the optical properties of different types of fractionated aerosols in  
21 western YRD. The total aerosols, mostly composed by scattering components (93.8%), have a mean  
22 optical depth of 0.65 at 550nm and refractive index of  $1.44+0.0084i$  at 440 nm. The fine aerosols are  
23 approximately 4 times more abundant and have very different compositions from coarse aerosols. The  
24 absorbing components account for only ~4.6% of fine aerosols and 15.5% of coarse aerosols and have

25 smaller sizes than the scattering aerosols within the same mode. Therefore, fine particles have stronger  
26 scattering than coarse ones, simultaneously reflecting the different size distributions between the  
27 absorbing and scattering aerosols. The relationships among the optical properties quantify the aerosol  
28 mixings and imply that approximately 15% and 27.5% of the total occurrences result in dust and black  
29 carbon dominating mixing aerosols, respectively, in the western YRD. Unlike the optical properties, the  
30 size distributions of aerosols in the western YRD are similar to those found at other sites over eastern  
31 China on a climatological scale, peaking at radii of 0.148 and 2.94  $\mu\text{m}$ . However, further analysis  
32 reveals that the coarse-dominated particles can also lead to severe haze pollution over the YRD.  
33 Observation-based estimations indicate that both fine and coarse aerosols in the western YRD exert a  
34 negative DRF, and this is especially true for fine aerosols ( $-11.17 \text{ W/m}^2$  at the top of atmosphere, TOA).  
35 A higher absorption fraction leads directly to the negative DRF being further offset for coarse aerosols  
36 ( $-0.33 \text{ W/m}^2$ ) at the TOA. Similarly, the coarse mode DRF contributes to only 13.3% of the total  
37 scattering aerosols but  $>33.7\%$  to the total absorbing aerosols. Sensitivity analysis states that aerosol  
38 DRFs are not highly sensitive to their profiles in clear-sky conditions. Most of the aerosol properties  
39 and DRFs have substantial seasonality in the western YRD. The results further reveal the contributions  
40 of each component of the different size particles to the total aerosol optical depths (AODs) and DRFs.  
41 Additionally, these results can be used to improve aerosol modelling performance and the modelling of  
42 aerosol effects in the eastern regions of China.

43

## 44 **1 Introduction**

45 Atmospheric aerosols have significant influences on air quality, human health, and regional/global  
46 climate changes. Scientists have suggested that scattering aerosols could greatly offset the warming

47 effects of greenhouse gases (Kiehl and Briegleb, 1993) while absorbing aerosols might further  
48 exacerbate global warming (Jacobson 2002). The global mean direct radiative forcing (DRF) of  
49 scattering aerosols, fossil fuel black carbon (BC) and all aerosols was estimated to be approximately  
50  $-0.55$ ,  $+0.2$  and  $-1.04$   $\text{W/m}^2$ , respectively (Forster et al., 2007; Reddy et al., 2005), at the top of  
51 atmosphere (TOA), thus changing atmospheric circulations and the hydrological cycle in different  
52 ways (Menon et al., 2002; Wang et al., 2015).

53 Many studies of aerosol radiative forcing and its climate effects have been carried out over the  
54 past two decades at both global and regional scales based on model simulations and observations (e.g.,  
55 Penner et al., 2001; Bellouin et al., 2003; Liao and Seinfeld, 2005; Wu et al., 2012; Wang et al., 2015;  
56 etc.); however, large uncertainties remain. Forster et al. (2007) noted that the global mean DRF varied  
57 from  $+0.04$  to  $-0.63$   $\text{W/m}^2$  for total aerosols and from  $+0.1$  to  $+0.3$   $\text{W/m}^2$  for BC. The ranges were  
58 larger at regional scales, especially in high aerosol emission regions (Zhuang et al., 2013a). The DRF  
59 uncertainties subsequently result in large biases of the aerosol-related climate effects. There are many  
60 factors that affect the simulated radiative forcing, including the aerosol optical properties, which are  
61 related to aerosol emissions, size distributions, profiles, compositions, and mixing states (Holler et al.,  
62 2003; Ma et al., 2017), as well as the surface albedo and clouds (Ma and Yu, 2012; Forster et al., 2007).  
63 The related uncertainties could be substantially reduced if the observed aerosol optical properties were  
64 determined and used (Forster et al., 2007).

65 With the rapid increase in population and economic growth, air pollutant emissions are much  
66 higher in East Asia than in other regions (Zhang et al., 2009). Additionally, dust aerosols from desert  
67 regions are always transported to northern and eastern China or even further afield (Wang et al., 2009;  
68 Sun et al., 2012; Li et al., 2015a). Consequently, aerosols in China frequently experience large loadings

69 and complicated compositions and spatial distributions (Zhang et al., 2012), especially in urban  
70 agglomerations or megacities (e.g., the Yangtze River Delta, YRD). Therefore, the aerosol optical  
71 properties in the YRD must be clarified via observations, which is a premise for accurately estimating  
72 the radiative effects of aerosols and for improving aerosol model performance over the eastern region  
73 of China. Recently, numerous observation-based studies have been conducted on both surface (e.g.,  
74 Bergin et al., 2001; Xu et al., 2002; Zhang et al., 2004; Xia et al., 2007; Yan et al., 2008; He et al., 2009;  
75 Fan et al., 2010; Cai et al., 2011; Xu et al., 2012; Wu et al., 2012; Zhang et al., 2015; Yu et al., 2016;  
76 Deng et al., 2016; Zhuang et al., 2017; etc.) and columnar (e.g., Chiang et al., 2007; Pan et al., 2010;  
77 Yu et al., 2011; Zhao et al., 2013; Tao et al., 2014; Zhu et al., 2014; Che et al., 2011; 2013; 2014; 2015a,  
78 b, c; 2017; Xia et al., 2016; Zheng et al., 2016; Qi et al., 2016, etc.) aerosol optical properties (and  
79 DRFs), especially in China. However, surface data cannot completely represent the total conditions of  
80 aerosols in the atmosphere as these aerosols are highly affected by the variations in boundary layers.  
81 The related deficiency could be solved with measurements of the columnar aerosols. For studies of  
82 surface aerosols, people mainly focus on the aerosol absorption coefficient (AAC) and scattering  
83 coefficient (SC). For columnar aerosol observations, the detailed aerosol optical and physical properties  
84 can be obtained, including the aerosol optical depth (AOD), refractive index, Ångström exponent (AE),  
85 etc. Che et al. (2015a) introduced a systematic long-term measurement of the countrywide total AOD  
86 and AE in China from 2002 to 2013 and indicated that the annual mean AODs were 0.14, 0.74 and 0.54  
87 for rural sites, urban sites, and eastern China, respectively. There are also some researches focusing on  
88 the aerosol optical properties in the YRD (Pan et al., 2010; Yu et al., 2011; Zhuang et al., 2014a; Qi et  
89 al., 2016). In addition to the aerosol optical properties, the observation-based aerosol DRFs have also  
90 been estimated around the world (such as those found in Markowicz et al., 2008; Khatri et al., 2009;

91 Kuhlmann and Quaas, 2010; Alam et al., 2011, Zhuang et al., 2014a, and Xia et al., 2016). However,  
92 almost all these investigations focused on the total aerosol forcing. For example, Xia et al. (2016)  
93 stated that the regional mean aerosol DRF in China was approximately  $-16\sim-37$  W/m<sup>2</sup> at the TOA and  
94 approximately  $-66\sim-111$  W/m<sup>2</sup> at the surface when the solar zenith angle was approximately 60°.

95 Although considerable studies of the observed columnar aerosol optical properties have been  
96 carried out in China and even within the YRD (one of the regions with the fastest urbanization in  
97 China), gaps in the current observations remain, especially in the urban areas of those regions with  
98 intensive human activities. In the YRD or eastern China, most of the investigations of the aerosol  
99 optical properties have focused on the coastal, lake and rural regions (Pan et al., 2010; Yu et al., 2011;  
100 Che et al., 2015a; Qi et al., 2016) of the central to eastern YRD. Additionally, most of these studies  
101 address only the total aerosol optical properties (independent of modes and compositions), except for  
102 the work of Qi et al. (2016). They also introduced the aerosol physical parameters and size fractional  
103 SSA of an eastern coastal city (Hangzhou, hereinafter written as urHZ) of the YRD, which is  
104 approximately 300 km away from the western YRD. As implied in Zhang et al. (2012), aerosols have  
105 complicated compositions and spatial distributions, especially in rapidly developing regions (such as  
106 YRD). Thus, considerable differences might exist in the aerosol optical and physical properties among  
107 the sites within the YRD. Additionally, none of research mentioned above studied the aerosol DRFs.  
108 Some investigations of the columnar aerosols in the western YRD (urNJ) were carried out by Zhuang et  
109 al. (2014a), but significant issues (not considered in their work) still require further study, such as the  
110 size fractional optical parameters and the DRFs of different aerosol components, as well as the aerosol  
111 physical properties of the different size fractions. Therefore, a more integrated investigation of the  
112 aerosol optical and physical properties, as well as their DRFs in the YRD, is still required. In this study,

113 the unaddressed issues for the western and whole YRD region mentioned above will be studied based  
114 on the measurements of a Cimel sun photometer in urNJ combined with a radiation transfer model  
115 (TUV, Madronich, 1993). Additionally, the aerosol types and mixings in the region will be further  
116 identified and discussed based on the relationships among the aerosol optical properties. Third, the  
117 observed aerosol profiles, which have not previously been considered in the YRD, are discussed and  
118 used to calculate the aerosol DRFs. The results of this study will be advantageous to further  
119 understanding the characteristics of aerosols over the eastern region of China. Additionally, this work  
120 will help improve aerosol model performance as well as the modelled climatic effects in the relevant  
121 regions. First, the observed aerosol parameters can be used for data assimilation to obtain more  
122 accurate inputs (including improved initial conditions and air pollutant emissions) for the model (Jiang  
123 et al., 2013 and Peng et al., 2017). Second, more precise aerosol refractive indexes and size  
124 distributions used in these numerical models will yield more reasonable aerosol loadings and DRFs  
125 (Ma et al., 2017). Third, both the aerosol optical properties and DRFs can be used to validate the  
126 simulations.

127 The methods are described in Section 2. The results and discussions are presented in Section 3,  
128 followed by the conclusions in Section 4.

129

## 130 **2 Methodologies**

### 131 **2.1 Sampling station and instruments**

132 The observation site (Urban Environmental Monitoring Station of Nanjing University) is located  
133 in the downtown area of Nanjing City (hereafter shortened to urNJ; located at 32.05° N, 118.78° E) in  
134 the western YRD. The site is on the roof of a 79.3-m-tall building, surrounded by few higher obstacles

135 and with no industrial pollution sources within a 30 km radius. However, there are several main roads  
136 with apparent traffic pollution. Detailed information about the site is available from Zhu et al. (2012).

137 The columnar aerosol optical properties and physical characteristics of the site were measured by  
138 a Cimel sun photometer (CE-318, Holben et al., 1998) during the period from Apr 2011 to Feb 2014.  
139 Routine maintenance and calibration was performed during the observational period. Due to  
140 malfunctions of the instrument and problems with data transmission, the data from May to Sep 2012  
141 and from Aug to Dec 2013 are invalid and were thus excluded. The wavelength-dependent AOD and  
142 AE of the total aerosols were directly measured by CE-318, while the following variables, including  
143 the aerosol size distributions; fractionated (fine and coarse) aerosol effective radius ( $R_{\text{eff}}$ ); mean radius  
144 ( $R_{\text{mn}}$ ), volume concentrations (Vol); wavelength-dependent optical depths of the various sizes of  
145 scattering, absorbing and total aerosols; aerosol SSA; and the wavelength-dependent refractive indices,  
146 are derived from the DOBVIC algorithm Version 2 (Dubovik et al., 2000; 2006). This algorithm has  
147 been widely used by the Aerosol Robotic Network (AERONET) and the China Aerosol Remote  
148 Sensing Network (CARSNET), while the products have been used globally, as introduced in the  
149 Introduction, due to their high accuracies. The errors for the AOD, absorption AOD (AAOD) and SSA  
150 are 0.01, 0.01 and 0.03, respectively (Yu et al., 2011; Li et al., 2015c). The errors of the fine and coarse  
151 aerosol SSAs are 0.037 and 0.085, respectively (Xu, 2015). The errors of the refractive index are 0.04  
152 for the real part and 0.0025-0.0042 for the imaginary part (Yu et al., 2011). Additionally, the error of  
153 the volume size distribution is less than 10% in the peak regions but is approximately 35% in valley or  
154 interval regions for the fine and coarse modes (Yu et al., 2011). Detailed descriptions of CE-318 and  
155 the corresponding observations from CARSNET are available from Li et al. (2015a) and Che et al.  
156 (2015a). For comparison, the 550 nm AODs and SSAs are calculated based on the given AODs at other

157 wavelengths and AEs (Angstrom. 1929):

$$158 \quad AOD_{550nm} = AOD_{440nm} \times \left(\frac{550_{nm}}{440_{nm}}\right)^{-AE_{440/870nm}} \quad (1)$$

$$159 \quad AAOD_{550nm} = AAOD_{440nm} \times \left(\frac{550_{nm}}{440_{nm}}\right)^{-AAE_{440/870nm}} \quad (2)$$

$$160 \quad SSA_{550nm} = \frac{AOD_{550nm} - AAOD_{550nm}}{AOD_{550nm}}. \quad (3)$$

161 For a further comparison, concurrent observations of the surface total AAC and AE measured by a  
162 7-channel Aethalometer (model AE-31, Magee Scientific, USA, Hansen et al., 1984; Weingartner et al.,  
163 2003 and Arnott et al., 2005) are used. The detailed calculations and corrections of the AAC at the site  
164 were presented by Zhuang et al. (2015). Additionally, the monthly mean AOD and AE of the total  
165 aerosols from the satellite-based Moderate Resolution Imaging Spectroradiometer (MODIS) were used  
166 in the analysis.

167 Based on the observed wavelength-dependent aerosol optical properties, the DRF of the aerosols  
168 in urNJ is investigated using the radiation transfer model TUV (Madronich, 1993). Only clear-sky  
169 DRFs are addressed here because almost all the measurements are carried out in free sky conditions.  
170 The solar component of the radiative transfer scheme in the TUV model follows the  $\delta$ -Eddington  
171 approximation. In addition to the aerosol optical properties, the surface albedo (Palancar and Toselli,  
172 2004) and aerosol vertical profiles (Forster et al., 2007) might also have significant influences on the  
173 DRF. Thus, the wavelength-dependent surface albedo from MODIS, the annual and seasonal mean  
174 aerosol profiles from the Cloud-Aerosol Lidar and Infrared Pathfinder Satellite Observations  
175 (CALIPSO) and the Polarization-Raman Lidar (PRL) in Nanjing are included when assessing the  
176 aerosol DRF. The aerosol DRF in this study is defined as the difference in the net shortwave radiative  
177 fluxes when including or excluding the aerosol effects at the TOA and surface. The gas absorptions in



178 the atmosphere were set to be constant. The scattering aerosol SSA was set to 0.9999 (similar to that of  
179 sulfate or nitrate, Li et al., 2015b) when calculating its DRF. The DRF of the absorbing aerosols is  
180 derived from the differences between the total and scattering aerosol DRFs.

181

## 182 **3 Results and discussions**

### 183 **3.1 Optical properties of the aerosols**

184 Unless otherwise specified, the AODs, SSAs and refractive indices of the aerosols hereinafter all  
185 represent the ones at 550, 550 and 440 nm, respectively. In addition to the total aerosols, the  
186 size-dependent (i.e., the fine and coarse fractions) aerosol optical properties of the different types  
187 (scattering and absorbing aerosols) are also discussed in this section. Therefore, there are nine types of  
188 aerosols: total aerosols (TA), total fine aerosols (FA), total coarse aerosols (CA), scattering aerosols  
189 (SA), fine scattering aerosols (FSA), coarse scattering aerosols (CSA), absorbing aerosols (AA), fine  
190 absorbing aerosols (FAA), and coarse absorbing aerosols (CAA).

191 Table 1 summarizes the statistics of the aerosol optical properties during the study period in urNJ.  
192 The mean total aerosol AOD is 0.65, and the SA's account for as much as 93.8% of this category. Fine  
193 mode AOD (FAOD), fine mode scattering AOD (FSAOD) and fine mode absorbing AOD (FAAOD)  
194 account for 81.53%, 81.97% and 56.09% of the total AODs, scattering AODs (SAODs) and absorbing  
195 AODs (AAODs), respectively, implying that coarse aerosols absorb more than fine ones. The 440/870  
196 nm AE of the total, scattering and absorbing aerosols are approximately 1.20, 1.19, and 1.32,  
197 respectively. Fine aerosols have much higher AEs, which can be 0.4-0.5 greater than those of the total  
198 aerosols. Overall, the absorbing aerosols have smaller sizes than the scattering ones in all modes,  
199 especially in the coarse mode, which is consistent with the results from the surface aerosols at the site

200 (Zhuang et al., 2017). The mean SSA of TA, FA and CA is 0.93, 0.95 and 0.82, respectively, further  
201 implying that the coarse aerosols have different compositions than the fine aerosols. The comparisons  
202 also indicate that surface aerosols (SSA=0.9 in Zhuang et al., 2017) are slightly more absorptive than  
203 the columnar aerosols in urNJ. The mean 440 nm refractive index is approximately  $1.44+0.0084i$ .

204 Table 1

205

### 206 **3.1.1 Seasonal variations in the aerosol optical properties**

207 Figure 1 presents the monthly variations in the AOD (a), SAOD (b) and AAO (c) as well as the  
208 contributions of their fine and coarse modes to their corresponding totals. The temporal variations in  
209 the total aerosol AOD are consistent with those of SAOD due to the significantly large ratio of  
210 SAOD/AOD. The AODs are all considerably high in the winter due to the more intense emissions of  
211 trace gases and particles (Zhang et al., 2009). Additionally, they are also high in spring and summer  
212 under the influences of dust, high efficiencies of moisture absorption growth and chemical  
213 transformation (Li et al., 2015a). Therefore, the seasonal variations of the total AODs are not so  
214 obvious in urNJ in the western YRD. These influences are prominent in the AOD seasonality for  
215 different aerosol types within the different size segments. The largest AODs appear in the spring for the  
216 coarse aerosols, whereas they appear in the summer for the fine aerosols in urNJ. The figure also  
217 implies that the scattering aerosols might have different size distributions than the absorbing aerosols.  
218 The fine mode fraction is 0.83 (peaking at 0.97) for scattering aerosols and is 0.56 (peaking at 0.83) for  
219 absorbing aerosols. It's noting that AOD in August does not include the ones in 2012 and 2013.  
220 Coincidentally, air pollution has been controlled since 2012 in Nanjing due to hosting international  
221 events in Aug 2013 and 2014. August AOD in 2011 is 1.18, much higher than those in 2012 (0.75) and

222 2013 (0.63) as referred from the MODIS retrievals. As a result, the AOD in August shown in Figure 1  
223 is “unusually” high.

224

225 Figure 1

226

227 The aerosol AEs also have substantial seasonal variations, especially for the absorbing aerosols, as  
228 illustrated in Figure 2. The seasonal variation of the fine aerosol AE is highly consistent with the coarse  
229 one for the absorbing aerosols while it is opposite for the scattering aerosols. Nevertheless, all AEs in  
230 the summer are the closest to 0 possibly due to the effects of high RH (Zhuang et al., 2014a). The  
231 whole mode AE of each aerosol type is determined by the both variations in the AEs in each mode and  
232 the fine mode fraction. Therefore, the smallest AEs appear in the summer (0.74 in July) for the total  
233 absorbing aerosols but appear in the spring (0.94 in Mar) for the total scattering aerosols. Similarly, the  
234 total aerosol AE is determined by both the variations of each aerosol type’s AE and the ratio of the  
235 scattering (or absorbing) aerosols to the total. And the seasonality of the total aerosol AEs is more  
236 consistent with that of the scattering aerosols. The figure also indicates that the scattering aerosols have  
237 much larger sizes than the absorbing aerosols, especially those in the coarse mode. Further comparisons  
238 indicate that the seasonal variations of the columnar SAE and AAE are consistent with their surface  
239 ones (Zhuang et al., 2017) at the site.

240

241 Figure 2

242

243 In addition to AOD and AE, the monthly variations in the aerosol SSAs and refractive indices are

244 also investigated, as shown in Figure 3. SSA is affected by both scattering and absorbing aerosols, as  
245 well as their relative contributions. The fine particles have much stronger scatterings than the coarse  
246 aerosols. Their SSAs have relatively weaker seasonality. Overall, both FSSA and CSSA are relatively  
247 smaller in the warmer seasons, although they were considerably large in August 2011. The total aerosol  
248 SSA is somewhere between the FSSA and CSSA and depends on the ratios of the FAOD to AOD. Thus,  
249 these SSAs have different seasonal variations from the FSSA or CSSA. SSA is also rather small in  
250 spring due to the largest contribution of coarse aerosols occurring in this season. The aerosol refractive  
251 indices also show considerable seasonality. The real part is large in the spring but small in the summer,  
252 which is similar to what was observed in Taihu Lake in the central YRD (Yu et al. 2011). The  
253 imaginary parts show relatively weaker seasonal variations than the real parts.

254

255 Figure 3

256

257 To provide a more quantitative knowledge, Table 2 summarizes the abovementioned seasonal  
258 means with the corresponding standard deviations for all the aerosol optical properties. And it's more  
259 obviously reflecting the different variations of the optical properties among different aerosol categories.  
260 For example, CAOD, CSAOD, CAAOD account for the majority of the AOD, SAOD and AAOD in  
261 the spring, with ratios of 30.1%, 27.9%, and 58.1%, respectively. FAOD, FSAOD, FAAOD account for  
262 the majority of the AOD, SAOD and AAOD in the summer, with ratios of 90.5%, 91.2% and 70.2%,  
263 respectively. Comparisons indicate that the seasonal variations of the optical properties are highly  
264 spatially inhomogeneous within the YRD. As indicated by Che et al. (2015a) and Qi et al. (2016), the  
265 largest AOD was found in the spring, while the lowest one appeared in the summer in urHZ, another

266 city on the eastern coast of the YRD. In Taihu Lake, a rural site in the central YRD, the lowest AOD  
267 appeared in the winter (Pan et al., 2010; Yu et al., 2011). Additionally, the aerosols absorb the most in  
268 the winter in the central regions of the YRD (Taihu Lake and urHZ), and their SSAs are as small as  
269 0.88 (Yu et al., 2011 and Qi et al., 2016). The aerosols in the western YRD (urNJ) are more scattering  
270 than those of the preceding areas. Nevertheless, AE variations are more consistent with each other  
271 between these sites, being smallest in the spring and largest in the fall.

272 Table 2

273

### 274 **3.1.2 Frequencies of the aerosol optical properties**

275 All AODs and SSAs follow a near lognormal pattern, and almost all the AEs and refractive  
276 indices follow a unimodal pattern (Figure 4). The ranges around their means are dominant, accounting  
277 for at least 60% of the total data samples during the entire study period. Similar to the temporal  
278 variations, the frequency distributions of the total aerosols (not shown) are also highly similar to those  
279 of the scattering aerosols in both the fine and coarse modes. The frequencies of the absorbing aerosol  
280 AEs differ from those of the scattering aerosol AEs. The occurrences of smaller CAAE (or large FAAE,  
281 AAE) values are also relatively high. Due to different absorbed fractions among coarse, fine and total  
282 aerosols, the curve of CSSA (FSSA) has a leftward (rightward) shifting compared with that of SSA,  
283 peaking around 0.84 (0.97). The fine aerosol SSAs were concentrated in a more narrow range (~0.1)  
284 than the CSSAs were (~0.3). For the refractive index, the frequencies peak around 1.42 and 0.008 for  
285 the real and imaginary parts, respectively, in urNJ during the study period. The frequency patterns of  
286 the aerosol optical properties also have substantial seasonality (not shown here). Overall, the curves  
287 shift leftward in low value seasons and rightward in high value seasons. In the summer, the AOD

288 curves might even have two peaks for the scattering or total aerosols, which are similar to the  
289 observations in Taihu Lake (Yu et al., 2011).

290

### 291 **3.1.3 Comparisons with MODIS AOD, AE and surface aerosols**

292 The AOD and AE observed by CE-318, to degrees, are well correlative with those from MODIS in  
293 terms of their seasonal variations and magnitudes (Figure 5). The linear correlation coefficients are  
294 0.71 and 0.67 between the monthly mean CE-318 and MODIS AODs and between the monthly mean  
295 CE-318 and MODIS AEs, respectively. The AOD from MODIS is greater (~1.2 times) than that from  
296 CE-318, with an average value of 0.80 during the study period. The slop of the linear fitting is 1.12 for  
297 AOD in urNJ, similarly to that in central China (slope=1.16, Dong et al., 2013). The mean AE at  
298 412/470 nm from MODIS is approximately 1.42. The standard deviations of the AOD and AE values  
299 are much larger for CE-318 than for MODIS, possibly due to the higher temporal resolution of the  
300 CE-318 observations.

301

302 Figure 5

303

304 The columnar AAOD and AAE values from CE-318 are less related to the surface aerosol  
305 absorption coefficient (AAC) and AAE from AE-31 (Figure 6). Because surface aerosols are mainly  
306 affected by local and regional emissions, and their loadings are highly related to the degrees of  
307 boundary layer development (Zhuang et al., 2014b and 2015). The columnar AAODs could be further  
308 affected by emissions and transports in the upper atmosphere. The surface AAE is concentrated in a  
309 narrower range and is larger (1.6) than that from CE-318. The linear correlation coefficients between

310 the AAOD and AAC and between the columnar and surface AAEs are 0.39 and 0.41, respectively,  
311 which are slightly worse than those between FAAOD and AAC (0.46) and between the columnar  
312 FAAE and surface AAE (0.47).

313

314 Figure 6

315

### 316 **3.1.4 Brief discussions**

317 Results here allow us to better understand the characteristics of the aerosols in the YRD. And they  
318 might be also useful for improving aerosol model performances and their radiative effects in the YRD  
319 or eastern China as referred in Introduction.

320 Most studies of the aerosol optical properties in China mainly focus on the AOD and AE of the  
321 short-term total aerosols (i.e., episodes, Che et al., 2013; Zheng et al., 2016; Che et al., 2015b),  
322 although the annual (Yu et al., 2011) and decadal (Che et al., 2015a) scale aerosols have been also  
323 carried out in recent years based on CE-318 measurements. Results here show that the mean AOD in  
324 urNJ is greater than those in northern China and the PRD but is smaller than those of the coastal cities  
325 of the YRD. The AE is larger in urNJ than in northern and central China. Che et al. (2015a) further  
326 suggested that those aerosols in urban areas likely had larger AODs and AEs than those in mountain  
327 and desert areas. It's the same in urNJ. Qi et al. (2016) showed that the aerosol SSAs at 440 nm in  
328 urHZ are approximately 0.90, 0.92 and 0.70 for the total, fine and coarse aerosols, respectively, also  
329 implying that the coarse aerosols absorb more than the fine ones. Our measurements show similar  
330 results. However, the aerosols in urNJ scatter more than those in urHZ in both the fine and coarse  
331 modes, also revealing the inhomogeneous distributions of the aerosol compositions in the YRD. This

332 study further augments the current observations of the aerosol optical properties in the YRD compared  
333 with previous studies.

334

### 335 **3.2 Physical properties of the aerosols**

336 In addition to the optical properties, the aerosol physical properties, including the volume size  
337 distributions, mode-dependent sizes (radius) and volume concentrations, were also retrieved. Figure 7  
338 shows the volume size distributions of the aerosols in different seasons (Figure 7a) and at different  
339 AOD (or polluted) levels (Figure 7b) in urNJ. It shows that the aerosols in urNJ have a typical bimodal  
340 structure in their volume size distributions in all seasons, presenting two-mode lognormal distributions  
341 in both the fine (radius  $< 0.6 \mu\text{m}$ ) and coarse modes (radius  $> 0.6 \mu\text{m}$ ). Their annual peaks appear at  
342 radii of  $0.148 \mu\text{m}$  for the fine mode and  $2.94 \mu\text{m}$  for the coarse mode. The aerosol volume size  
343 distributions also have substantial seasonality. Dust episodes lead to the peak values in the spring being  
344 much smaller in the fine mode than those in the coarse mode, which is the opposite trend than in the  
345 other seasons (especially in the summer). Therefore, the mean radius of the aerosols increases  
346 significantly in the spring due to the high proportion of coarse particles, leading to a smaller AE, as  
347 discussed in the previous sections. In the summer, the curve has a rightward shift, showing a larger  
348 aerosol size in both the fine and coarse modes due to the high hygroscopic growth efficiency. The fine  
349 particles are dominant in the summer and result in large AE values, opposite to the patterns in the  
350 spring. The aerosol volume size distribution varies with different AOD values (Figure 7b) in urNJ.  
351 Overall, the peak value has a substantial rightward shift with increasing AOD for fine aerosols while a  
352 slightly leftward shift for coarse aerosols, implying that the growth of the fine aerosols is advantageous  
353 to enhance the aerosol radiative effect. In urNJ, both fine and coarse particles have approximately the



354 same levels when AOD is below  $\sim 0.8$ . In addition, the fine aerosols begin to dominate more when  
355  $AOD > 0.8$ . The results here are mostly consistent with the ones from Yu et al. (2011), Qi et al. (2016),  
356 and Zheng et al. (2016). However, the figure here further indicates that both fine and coarse particles  
357 themselves might cause very serious haze pollutions in YRD, showing considerably high peak values  
358 in both fine and coarse modes, which has not been observed in previous publications. The aerosol size  
359 distributions here are also very useful for optimizing numerical models.

360

361 Figure 7

362

363 To further investigate the physical features, the seasonal variations in the aerosol effective and  
364 mean radius and the volume concentrations in urNJ are presented in Figure 8. The mean effective  
365 radius, which is generally smaller than the mean one in all modes, is approximately 0.34, 0.16, and  
366  $2.18 \mu\text{m}$  for the total, fine and coarse aerosols, respectively, during the study period. The seasonal  
367 variations in the radii have a strong anti-correlation to that of the AEs (Figure 2). Both the fine and  
368 coarse aerosol radii are larger in the summer than in the other seasons while the total aerosol radius is  
369 much larger in the spring. Unlike the radius, the seasonal variations in the volume concentrations of the  
370 fine and coarse aerosols are different, peaking in the spring for coarse aerosols and in the summer for  
371 fine aerosols. Although both the fine and coarse aerosols have the same annual volume levels in urNJ,  
372 their contributions to the total aerosol volumes vary significantly with season. The coarse aerosols lead  
373 directly to the largest total aerosol volume peaking in the spring.

374

375 Figure 8

376

### 377 **3.3 Aerosol classification based on optical properties**

378 The aerosol clusters, to a certain degree, can be identified based on the relationships between  
379 SSAs at 491 nm and AEs at 491/870 nm, between the real refractive index (RRI) at 670 nm and the AE  
380 at 491/870 nm, and between the SSA differences ( $dSSA = SSA_{870nm} - SSA_{491nm}$ ) and AE at 491/870 nm, as  
381 presented by Russell et al. (2014). They proposed a Mahalanobis Classification based on “a priori”  
382 information for each type of aerosol source (e.g., dust, urban, biomass aerosols). Different aerosols  
383 would then be mostly concentrated within the corresponding ellipses of a two-dimensional scatter plot  
384 of SSA versus AE (or RRI versus AE, or  $dSSA$  versus AE). Based on their classifications, aerosols  
385 from pure dust, polluted dust, biomass burning, industrial urban, developing urban, and marine sources  
386 (Figure 8 in Russell et al., 2014) can be identified. For example, the polluted dust aerosols are mostly  
387 within the ellipses with smaller AE (near 1.0) values, relatively small SSA levels (0.85 to 0.95), and  
388 much larger real refractive indices (1.45 to 1.55) and SSA differences (0 to 0.05) than those present for  
389 other aerosols. The aerosols from a developing urban area generally have smaller sizes than polluted  
390 dust (AE ranging from 1 to 1.6), but they have larger SSA (0.9 to 1.0) values, smaller real refractive  
391 indices (1.4 to 1.5) and smaller SSA differences (approximately 0). More classifications can be found  
392 in (Russell et al., 2014). Based on their classification standards, the aerosols in urNJ could be basically  
393 identified as clusters of polluted dust, developing urban and industrial urban during the sampling period,  
394 as shown in Figure 9, which further supports the analysis in Section 3. Although urNJ is only  
395 approximately 300-400 km away from the East China Sea, few marine or sea salt aerosol components  
396 are observed, as illustrated in Figure 9. Unfortunately, the observations missed a biomass burning event  
397 in Jun 2012 (Zhuang et al., 2014b, 2015) because the instrument was having maintenance performed.

398 Otherwise, the figure would be more comprehensive. Analysis here might help us understand the  
399 aerosol sources, transformations, transports and radiative effects in the YRD. In addition, this  
400 information also indicates that the Mahalanobis Classification is a very useful approach for classifying  
401 aerosol into types, especially in cases of data shortages or insufficient methods. However, this method  
402 still has a limitation. The classified ellipses have some overlaps among different aerosols clusters. In  
403 overlap regions, classifying the aerosols into types is a challenge. For example, it is not easy to  
404 distinguish between polluted dust aerosols with large AE values and urban aerosols with smaller AE.  
405 Therefore, if there are two kinds of aerosols with nearly identical coordinates, further information is  
406 needed, or a more effective approach should be taken into account.

407

408 Figure 9

409

410 In addition to the types, the aerosol mixtures/compositions can also be identified based on SSA  
411 and AAOD. Generally, dust aerosols have strong absorption in the ultraviolet (UV) band but become  
412 non-absorbing in the visible band, leading to SSAs increasing monotonically with the wavelength. For  
413 biomass burning aerosols, the SSAs decrease monotonically with wavelength. Non-monotonic  
414 variations in SSA with changes in wavelength might be due to aerosol mixtures dominated by another  
415 type of aerosol, as indicated by Li et al. (2015c). They proposed two curvature parameters to provide  
416 additional information on the aerosol compositions: the second derivative of the second-order  
417 polynomial fit of the SSA and wavelength and the fit of the AAOD and wavelength, as shown in Eq. 4  
418 and Eq. 5.

419 
$$\ln(SSA_{\lambda}) = \beta_2 \ln(\lambda)^2 + \beta_1 \ln(\lambda) + \beta_0 \quad (4)$$

420  $\ln(AAOD_\lambda) = \alpha_2 \ln(\lambda)^2 + \alpha_1 \ln(\lambda) + \alpha_0$  (5)

421 where  $-\beta_2$  and  $\alpha_2$  are the SSA curvature and AAOD curvature, respectively. Detailed descriptions  
422 were presented by Li et al. (2015c). Based on these parameters, the aerosols can be identified as dust  
423 dominated, BC (including biomass burning and urban/industrial aerosols) dominated and other mixed  
424 (peak) type aerosols because the curvature probability (or frequency) distributions are different for the  
425 different aerosol mixtures. As indicated in Li et al. (2015c), the SSA or AAOD curvature is mostly  
426 concentrated at approximately 0 for the BC-dominated aerosol mixture, which is much smaller than  
427 that of the dust-dominated aerosol mixtures (0.1 for SSA curvature and 0.5-1 for AAOD curvature)  
428 over East Asia. Based on their method, the curvatures of SSA and AAOD are calculated and then  
429 divided into three categories according to the monotonicity of the SSA. The results show that there are  
430 approximately 15.0%, 27.5% and 42.3% occurrences of monotonically increasing, decreasing and 670  
431 nm peaking SSA spectra, respectively, in urNJ. In addition, their probability (or frequency)  
432 distributions are plotted in Figure 10. The figure indicates that the SSA and AAOD curvature patterns  
433 are highly consistent with those in Li et al. (2015c) for the monotonic categories, which implies that the  
434 ~15% and ~27% samples with monotonically increasing and decreasing SSA spectra are the  
435 dust-dominated and BC-dominated mixing aerosols, respectively, in urNJ during the observed period.  
436 For example, a very strong dust storm from northwest China and Mongolia on 1st May 2011 (Li et al.,  
437 2015a) directly yielded mean SSA and AAOD curvatures of 0.12 and 1.11, respectively, which are  
438 close to the values (0.11 and 1.24, respectively) of the pure dust aerosols (Li et al., 2015c). For the rest  
439 of the categories with non-monotonic SSA spectra, the SSA curvatures are mostly concentrated from  
440 0.3 to 0.8, implying that the dust component might not exceed 10%, while the scattering species  
441 (organic carbon not included) accounted for at least 30% of the mixing particles in western YRD

442 according to the sensitivity results from Li et al. (2015c). Additional data are needed to derive further  
443 information. However, these results might help us gain a better understanding of the mixings of  
444 aerosols in the urban areas of the YRD. Similar to Russell et al. (2014), Li et al. (2015c) provided an  
445 effective approach for classifying the aerosol compositions based on a single data set (such as the  
446 CE-318 retrievals).

447

448 Figure 10

449

### 450 **3.4 The direct radiative forcing of the aerosols**

451 Based on the abovementioned wavelength-dependent optical properties combined with the  
452 observed surface albedo and aerosol profiles, the clear-sky size-dependent aerosol DRF of the fine and  
453 coarse components at both the TOA and the surface in urNJ are investigated using the radiation transfer  
454 model TUV (Madronich, 1993). Due to a lack of SSA observations of each aerosol component, the  
455 scattering aerosol DRF is estimated based on a given SSA value (0.9999, equal to that of sulfate or  
456 nitrate aerosol) in a reference (Li et al., 2015b). As indicated in the last section, the absorbing aerosols  
457 in urNJ are always in a mixed state. Therefore, the absorbing aerosol DRF cannot be estimated directly  
458 using the BC SSA. Here, this value is derived from the difference between the total and scattering  
459 aerosol DRFs, which might be more representative. For comparison, the aerosol DRF is also calculated  
460 based on the AAOs, AAEs and BC SSA (Li et al., 2015b).

461 Observational aerosol profiles, which have not have been used in previous investigations (e.g.,  
462 Zhuang et al., 2014a), might be important to the DRF estimations. Figure 11 shows the mean vertical  
463 aerosol profiles observed by CALIPSO (annual scale data) and the PRL (seasonal scale data) in

464 Nanjing. For further comparisons, all the profiles in the figure were standardized to percentages (%).  
465 The figure suggests that the ground and satellite-based aerosol profiles are substantially different. The  
466 CALIPSO profile is more homogeneous than the PRL one, accounting for approximately 61% and 88%,  
467 respectively, below 4 km. Due to the lack of the long-term measurement of PRL and the different  
468 products of the different observational platforms, both the CALIPSO and PRL profiles are used here.  
469 Additionally, a combined profile (grey line) of the averaged CALIPSO and PRL values is included and  
470 indicates that aerosols account for approximately 75% of the total below 4 km and approximately 60%  
471 in the boundary layer for the combined profile, which is somewhat similar to the default profile of TUV  
472 (Palancar and Toselli, 2004). All these four profiles were used when estimating the aerosol DRFs.

473

474 Figure 11

475

#### 476 **3.4.1 The aerosol direct radiative forcing in clear-sky conditions**

477 Hereinafter, DRFs, unless otherwise specified, represent the averaged values from CALIPSO,  
478 PRL and a combined profile-based forcing in clear-sky conditions. Figure 12 shows the seasonal  
479 variations in the size-dependent daytime TOA and surface DRFs of the total, scattering and absorbing  
480 aerosols in urNJ. The aerosol DRFs are highly dependent on the aerosol optical properties and  
481 compositions. Overall, the fine aerosols contribute considerably more to the total aerosol DRFs,  
482 especially for scattering aerosols. The coarse aerosol DRF accounts for only 13.3% for the scattering  
483 aerosols, while this fraction is >33.7% for the absorbing aerosols at both the TOA and surface in urNJ.  
484 Negative scattering aerosol DRFs could be significantly offset at the TOA and could be further  
485 strengthened at the surface by absorbing aerosols. Therefore, the total coarse aerosol DRF at the TOA

486 is very weak due to a much smaller CSSA and subsequently accounts for a much smaller contribution  
487 to the total aerosol DRF than the fine aerosols do. Both the scattering and absorbing aerosol DRFs have  
488 similar seasonality to their AODs. And the scattering aerosol DRFs have the same seasonality as the  
489 absorbing ones within the same mode. In addition to AODs, the surface albedo and solar zenith angle  
490 also have a strong influence on the variations in the aerosol DRFs. As implied by Zhuang et al. (2014a),  
491 a brighter surface would yield a weaker negative DRF and a stronger positive DRF, assuming a fixed  
492 AOD. The seasonal mean surface albedo averaged from four wavelengths (440, 670, 870 and 1020 nm)  
493 is approximately 0.145, 0.170, 0.129, and 0.137 in the spring, summer, fall, and winter, respectively. As  
494 a result, the scattering and fine absorbing aerosol DRFs are also strong in the winter and spring,  
495 respectively. Unlike those of the single aerosol types, the variations of the total aerosol DRFs are  
496 co-affected by those of both the scattering and absorbing aerosols. Thus, the strongest TOA DRF of the  
497 total fine aerosols appears in the winter instead of the summer, and the total coarse aerosol DRFs are  
498 positive at the TOA in the summer. For all modes, the seasonal variations of the total aerosol DRFs at  
499 the TOA are more consistent with those of the fine mode. Different from the TOA DRFs of the total  
500 aerosols, the surface DRFs are much more consistent with those of the corresponding AODs.

501

502 Figure 12

503

504 For further comparisons (Figure 13), the absorbing aerosol DRFs based on the observed AAOD,  
505 AAE and fresh BC SSA (Li et al., 2015b) are also used. Although the absorbing aerosol DRFs are  
506 estimated in different ways, they are highly correlated at both the TOA and surface, as shown in the  
507 figure. Apparently, the DRFs from the second method are much weaker than those from the first

508 calculation, possibly due to the absorbing aerosols in urNJ being in a constantly mixed state, as shown  
509 by the analysis in the previous section and as indicated by Zhuang et al. (2015). Jacobson (2000)  
510 suggested that the aged (mixed) absorbing aerosols have a much stronger ability to absorb solar  
511 radiation, by a factor of two. Zhuang et al. (2013a and 2013b) stated that the simulated regional mean  
512 TOA DRF of the mixed BC (+1.56 W/m<sup>2</sup>) over East Asia is approximately 1.9 times that of the  
513 unmixed BC. The ratio is approximately 1.73 in this study, implying that the absorbing aerosol DRF  
514 from the first method is reasonable. The comparison here further proves the importance of the mixing  
515 states in estimating the absorbing aerosol radiative effects.

516

517 Figure 13

518

519 Table 3 lists the annual mean size-dependent DRFs of the total, scattering and absorbing aerosols  
520 at both the TOA and the surface in urNJ. The DRFs at the surface are all stronger than those at the TOA.  
521 The mean DRFs are -10.69, -16.45, 5.76 W/m<sup>2</sup> at the TOA and -25.54, -21.37 and -8.38 W/m<sup>2</sup> at the  
522 surface for the TA, SA and AA, respectively. The fine mode TOA DRFs are nearly an order of  
523 magnitude stronger than those of the coarse mode for the total and scattering aerosols. The DRFs of the  
524 fine absorbing aerosols have the same order of magnitude but are stronger than those of the coarse  
525 absorbing aerosols. It's noting that the total DRFs in the table are not exactly the sum of the  
526 contributions from the fine and coarse ones, because the coarse aerosol affection on the solar radiation  
527 is excluded when calculating the fine aerosol DRF separately, and vice versa.

528 Table 3

529



530 Various studies of aerosol DRFs have been carried out based on observations or numerical models.  
531 Overall, the DRFs of urban aerosols are much stronger than those on regional or global scales. Forster  
532 et al. (2007) summarized the global mean clear-sky DRFs of the total observational aerosols as -5.4  
533  $\text{W/m}^2$ . Zhuang et al. (2013a and 2013b) indicated that simulated clear-sky DRFs are  $-4.97 \text{ W/m}^2$  for  
534 total aerosols and  $+1.2 \text{ W/m}^2$  for BC over East Asia. On a subregional or urban scale, the  
535 observation-based analysis showed that the total aerosol DRFs always exceeded  $10^1 \text{ W/m}^2$  (Markowicz  
536 et al., 2008; Khatri et al., 2009; Wang et al., 2009; Kuhlmann and Quaas, 2010; Alam et al., 2011; Che  
537 et al., 2015c, and so on). For example, the total aerosol DRF could be as strong as  $-25 \text{ W/m}^2$  over the  
538 Qinghai-Tibet Plateau (Kuhlmann and Quaas, 2010) and  $-30 \text{ W/m}^2$  in the north China Plain (Che et al.,  
539 2014 and 2015c). Our results show that the aerosols in the urban area of the western YRD could also  
540 exert very strong DRFs, reaching as high as  $-25.5 \text{ W/m}^2$  at the surface. Apparently, the DRFs here have  
541 smaller uncertainties than those from simulations because of the use of observations. And they might  
542 be also more precise compared with previous estimation in Zhuang et al. (2014a). This study further  
543 investigated the size fractional DRFs of different aerosol components in urban areas of the western  
544 YRD, which allows a better understanding of the effects of aerosols on solar shortwave radiation. In  
545 addition, these issues have not been addressed in previous studies. The results here can also be used to  
546 validate numerical simulations and to evaluate model performance concerning aerosol radiative effects.

547

#### 548 **3.4.2 Sensitivity of the aerosol direct radiative forcing to aerosol profiles**

549 Different aerosol profiles might result in different DRFs. Figure 14 presents the TOA and surface  
550 DRFs of different aerosol types, including the SA, AA and TA, based on four kinds of aerosol profiles  
551 from CALIPSO, PRL, the combined CALIPSO and PRL shown in Figure 11 and the default one from

552 TUV (Palancar and Toselli, 2004) in clear-sky conditions. The figure shows that the aerosol DRFs in  
553 clear-sky conditions are not very sensitive to the aerosol profile, although the absorbing aerosol TOA  
554 DRFs are more sensitive than those of the scattering aerosols. Overall, both the scattering and  
555 absorbing aerosol DRFs at the TOA become weaker to some extent when more aerosols are  
556 concentrated in the lower layers of the atmosphere, especially for the AA's. Here, a profile impact  
557 factor (PIF) is defined as the ratio of the standard deviations among the four types of DRFs in Figure  
558 14 to the averaged values of these four DRFs. The PIF is approximately 4.97% for the absorbing  
559 aerosol TOA DRF and is below 2% for the rest of the types of DRFs. In contrast, the aerosol profiles  
560 might have much stronger influences on the DRFs in cloudy sky conditions because the absorbing  
561 aerosols over brighter cloud will absorb more shortwave radiation (Podgorny and Ramanathan, 2001).  
562 This issue will be addressed in the future.

563

564 Figure 14

565

### 566 **3.4.3 Brief discussions**

567 Although the observation-based DRFs of the total, scattering and absorbing aerosols as well as  
568 their sensitivities to the aerosol profiles are analysed in this study, uncertainties still exist due to the  
569 measurement errors of the optical properties mentioned in Section 2. Additional estimations of the  
570 aerosol DRFs are carried out based on the errors of AOD, AAOD and SSAs. The results indicate that  
571 the greater uncertainties of the aerosol DRFs are mainly derived from the errors of SSA or AAOD. The  
572 uncertainty of the total aerosol AODs (0.01) yield only approximately 1% relative biases for the total  
573 aerosol DRFs at both the TOA and surface. The total or fine aerosol SSA errors (0.03 or 0.037,

574 respectively) may result in approximately 24% of the uncertainties at the TOA (<15% at the surface)  
575 for the corresponding DRFs. A larger coarse aerosol SSA error (0.085) leads to an ~24% uncertainty of  
576 its surface DRFs. AAOD errors (0.01) cause approximately 20% of the uncertainties for the absorbing  
577 DRFs at both the TOA and surface while accounting for only 1.2% of the scattering DRFs uncertainties.  
578 Overall, these uncertainties are smaller than those presented in the 5th IPCC report (IPCC, 2013) and  
579 could be further decreased if the measurements or the algorithms were fairly improved. For example,  
580 the absorbing aerosol DRFs would become more accurate if corresponding SSAs could be obtained by  
581 measurements. Also, the aerosol DRFs would be better estimated to a degree if its profiles with higher  
582 temporal resolution could be used in future. Additionally, extremely high aerosol loadings are  
583 frequently observed during serious pollution episodes, including dust storms, biomass burning, and  
584 regional transport (Zhuang et al., 2014a, b and 2015). The aerosol optical and physical properties as  
585 well as the radiative forcing are different during these extreme episodes, which also deserves further  
586 study.

587

#### 588 **4 Conclusions**

589 In this study, the size-dependent aerosol optical and physical properties observed by a Cimel sun  
590 photometer (CE-318), as well as the corresponding DRFs calculated by the radiation transfer model  
591 TUV based on observations from the urban area of Nanjing (urNJ), western YRD, are investigated.

592 In the urban area of the western YRD, the annual mean total aerosol AOD is 0.65 and is mostly  
593 due to the contribution of the scattering components (0.61). The absorption fraction is as small as  
594 ~6.7%. Approximately 80% of the aerosols in urNJ during the sampling period are fine mode aerosols.  
595 The absorption fraction is approximately 4.6% in the fine mode and 15.5% in the coarse mode,

596 showing the very different compositions and absorption characteristics of these two kinds of aerosols.  
597 Compared with the satellite retrievals, the observations show aerosol optical properties with much  
598 higher temporal resolutions and more products. Further analysis of the aerosol optical properties  
599 indicates that there might be approximately 15% and 27% occurrences of dust-dominated and  
600 BC-dominated mixing aerosols, respectively, in the western YRD during the study period.

601 The aerosols in the western YRD have a two-mode lognormal pattern in their volume size  
602 distribution, peaking at the radii of 0.148 and 2.94  $\mu\text{m}$  on an annual scale. The fine particles have the  
603 same contribution as the coarse ones when  $\text{AOD} < 0.8$ , and they become predominate when  
604  $0.8 < \text{AOD} < 1.4$ . Different from observations in other regions, the results here further reveal that the  
605 coarse aerosols might also induce very serious pollution episodes in the YRD. Both fine and coarse  
606 aerosols have the same levels of volume concentrations, although their radii differ by an order of  
607 magnitude.

608 Similar to AODs, the total fine aerosol DRF also have a much contribution to the totals, especially  
609 at TOA (>97%), with a value of  $-11.17 \text{ W/m}^2$ . However, differences exist. For each aerosol type, the  
610 coarse aerosol DRF accounts for only  $\sim 13.3\%$  for the scattering aerosols while at least 33.7% for the  
611 absorbing aerosols at both the TOA and the surface in urNJ. The DRFs estimated for urNJ in this study  
612 are much stronger than their regional or global means.

613 Most of the size-dependent aerosol optical and physical properties as well as their DRFs have  
614 significant seasonality in the western YRD. The DRF variations for each aerosol type within the same  
615 mode are mostly consistent with the variations in the corresponding AODs, peaking in the summer for  
616 the fine aerosols and in the spring for the coarse ones. However, the variations in the total aerosol  
617 DRFs at the TOA are different from the corresponding AODs because the negative DRFs of the

618 scattering aerosols are always offset by the absorbing aerosols. Both the fine and coarse aerosols have  
619 the largest sizes in the summer, which differs from the total aerosol mode (which peaks in the spring).

620 The sensitivities of clear-sky aerosol DRFs to the aerosol profiles are not significant and are all  
621 smaller than 5%. Overall, both the scattering and absorbing aerosol DRFs at the TOA would become  
622 somewhat weaker if more aerosols were concentrated in the lower layers of the atmosphere, especially  
623 for the absorbed DRF. Further investigation suggests that another uncertainty of the DRFs is from the  
624 measuring errors of the aerosol optical properties. The larger biases are mainly derived from the errors  
625 of the SSA and AAOD.

626

## 627 **5 Data availability**

628 The monthly mean optical depth (AOD) and Ångström exponent (AE) of the total aerosols from  
629 the satellite-based Moderate Resolution Imaging Spectroradiometer (MODIS) are accessible from  
630 <https://giovanni.gsfc.nasa.gov/giovanni/>.

631

632 *Competing interests.* The authors declare that they have no conflict of interest.

633

634 **Acknowledgements:** This work was supported by the National Key R&D Program of China  
635 (2017YFC0209803, 2014CB441203, 2016YFC0203303), the National Natural Science Foundation of  
636 China (41675143, 91544230, 41621005), and a project Funded by the Priority Academic Program  
637 Development of the Jiangsu Higher Education Institutions (PAPD). The authors would like to thank all  
638 members in the AERC of Nanjing University for maintaining instruments, and also thank the  
639 anonymous reviewers for their constructive and valuable comments on this paper.

640

641 **References**

642 Alam, K., Trautmann, T., and Blaschke, T.: Aerosol optical properties and radiative forcing over  
643 mega-city Karachi. *Atmos. Res.* 101, 773-782, 2011.

644 Angström, A.: On the atmospheric transmission of sun radiation and on dust in the air, *Geogr. Ann.*, 11,  
645 156–166, 1929.

646 Arnott, W. P., Hamasha, K., Moosmuller, H., Sheridan, P. J., and Ogren, J. A.: Towards aerosol  
647 light-absorption measurements with a 7-wavelength aethalometer: evaluation with a photoacoustic  
648 instrument and 3-wavelength nephelometer, *Aerosol Sci. Tech.*, 39, 17–29,  
649 doi:10.1080/027868290901972, 2005.

650 Bellouin, N., Boucher, O., Tanré, D., and Dubovik, O.: Aerosol absorption over the clear-sky oceans  
651 deduced from POLDER-1 and AERONET observations, *Geophys. Res. Lett.*, 30, 1748,  
652 doi:10.1029/2003GL017121, 2003.

653 Bergin, M. H., Cass, G. R., Xu, J., Fang, C., Zeng, L., Yu, T., Salmon, L. G., Kiang, C. S., Tang, X. Y.,  
654 Zhang, Y. H., and Chameides, W. L.: Aerosol radiative, physical, and chemical properties in Beijing  
655 during June 1999, *J. Geophys. Res.*, 106 (D16), 17969–17980, 2001.

656 Cai, H. K., Zhou, R. J., Fu, Y. F., Zheng, Y. Y., and Wang, Y. J.: Cloud-aerosol lidar with or thogonal  
657 polarization detection of aerosol optical properties after a crop burning case, *Clim. Environ. Res.*,  
658 16, 469–478, 2011.

659 Che, H. Z., Zhang, X. Y., Xia, X., Goloub, P., Holben, B., Zhao, H., Wang, Y., Zhang, X. C., Wang, H.,  
660 Blarel, L., Damiri, B., Zhang, R., Deng, X., Ma, Y., Wang, T., Geng, F., Qi, B., Zhu, J., Yu, J., Chen,  
661 Q., and Shi, G.: Ground-based aerosol climatology of China: aerosol optical depths from the China

662 Aerosol Remote Sensing Network (CARSNET) 2002–2013, *Atmos. Chem. Phys.*, 15, 7619–7652,  
663 2015a.

664 Che, H. Z., Zhao, H. J., Wu, Y. F., Xia, X. A., Zhu, J., Wang, H., Wang, Y. Q., Sun, J. Y., Yu, J., Zhang,  
665 X. Y., and Shi, G. Y.: Analyses of aerosol optical properties and direct radiative forcing over urban  
666 and industrial regions in Northeast China, *Meteorology and Atmospheric Physics*, 127(3), 345-354,  
667 doi:10.1007/s00703-015-0367-3, 2015c.

668 Che, H., Qi, B., Zhao, H., Xia, X., Goloub, P., Dubovik, O., Estelles, V., Cuevas-Agulló, E., Blarel, L.,  
669 Wu, Y., Zhu, J., Du, R., Wang, Y., Wang, H., Gui, K., Yu, J., Zheng, Y., Sun, T., Chen, Q., Shi, G.,  
670 and Zhang, X.: Aerosol optical properties and instantaneous radiative forcing based on high  
671 temporospatial resolution CARSNET ground-based measurements over eastern China, *Atmos.*  
672 *Chem. Phys. Discuss.*, <https://doi.org/10.5194/acp-2017-530>, 2017.

673 Che, H., Wang, Y., and Sun, J.: Aerosol optical properties at Mt. Waliguan observatory, China, *Atmos.*  
674 *Environ.*, 45, 6004–6009, 2011.

675 Che, H., Xia, X., Zhu, J., Li, Z., Dubovik, O., Holben, B., Goloub, P., Chen, H., Estelles, V.,  
676 Cuevas-Agulló, E., Blarel, L., Wang, H., Zhao, H., Zhang, X., Wang, Y., Sun, J., Tao, R., Zhang, X.,  
677 and Shi, G.: Column aerosol optical properties and aerosol radiative forcing during a serious  
678 haze-fog month over North China Plain in 2013 based on ground-based sunphotometer  
679 measurements, *Atmos. Chem. Phys.*, 14, 2125–2138, doi:10.5194/acp-14-2125-2014, 2014.

680 Che, H., Xia, X., Zhu, J., Wang, H., Wang, Y., Sun, J., Zhang, X., and Shi, G.: Aerosol optical  
681 properties under the condition of heavy haze over an urban site of Beijing, China, *Environ. Sci.*  
682 *Pollut. R.*, 22, 1043–1053, doi:10.1007/s11356-014-3415-5, 2015b.

683 Che, H., Wang, Y., Sun, J., Zhang, X., Zhang, X., and Guo, J.: Variation of Aerosol Optical Properties

684 over the Taklimakan Desert in China, *Aerosol Air Qual. Res.*, 13, 777–785, 2013.

685 Chiang, C. W., Chen, W. N., Liang, W. A., Das, S. K., and Nee, J. B.: Optical properties of tropospheric  
686 aerosols based on measurements of lidar, sun-photometer, and visibility at Chung-Li (25°N, 121°E),  
687 *Atmos. Environ.*, 41, 4128-4137, doi:10.1016/j.atmosenv.2007.01.019, 2007.

688 Deng, J. J., Zhang, Y. R., Hong, Y. W., Xu, L. L., Chen, Y. T., Du, W. J., and Chen, J. S.: Optical  
689 properties of PM<sub>2.5</sub> and the impacts of chemical compositions in the coastal city Xiamen in China,  
690 *Science of the Total Environment*, 557-558, 665-675, 2016.

691 Dong, Z. P., Li, X. M., Du, C. L., and Zhang, G. J.: Study on aerosol optical property in Xi'An Region,  
692 *Plateau Meteorology*, 32(3), 856-864, doi:10.7522/j.issn.1000-0534.2012.00079, 2013.

693 Dubovik, O. and King, M. D.: A flexible inversion algorithm for the retrieval of aerosol optical  
694 properties from Sun and sky radiance measurements, *J. Geophys. Res.*, 105, 20673–20696,  
695 doi:10.1029/2000JD900282, 2000.

696 Dubovik, O., Sinyuk, A., Lapyonok, T., Holben, B. N., Mishchenko, M., Yang, P., Eck, T. F., Volten, H.,  
697 Munoz, O., Veihelmann, B., van der Zande, W. J., Leon, J. F., Sorokin, M., and Slutsker, I.:  
698 Application of spheroid models to account for aerosol particle nonsphericity in remote sensing of  
699 desert dust, *J. Geophys. Res.-Atmos.*, 111, D11208, doi:10.1029/2005jd006619, 2006.

700 Fan, X. H., Chen, H. B., Xia, X. A., Li, Z. Q., and Cribb, M.: Aerosol optical properties from the  
701 Atmospheric Radiation Measurement Mobile Facility at Shouxian. China, *J. Geophys. Res.*, 115,  
702 D00K33, doi:10.1029/2010JD014650, 2010.

703 Forster, P., Ramaswamy, V., Artaxo, P., Berntsen, T., Betts, R., Fahey, D. W., Haywood, J., Lean, J.,  
704 Lowe, D. C., Myhre, G., Nganga, J., Prinn, R., Raga, G., Schulz, M., and Van Dorland, R.: Changes  
705 in atmospheric constituents and in radiative forcing, in: *Climate Change 2007: The Physical*



706 Science Basis. Contribution of Working Group I to the Fourth Assessment Report of the  
707 Intergovernmental Panel on Climate Change, edited by: Solomon, S. et al., Cambridge Univ. Press,  
708 Cambridge, UK, 129–234, 2007.

709 Hansen, A. D. A., Rosen, H., and Novakov, T.: The aethalometer: an instrument for the real time  
710 measurements of optical absorption by aerosol particles, *Sci. Total Environ.*, 36, 191–196, 1984.

711 He, X., Li, C. C., Lau, A. K. H., Deng, Z. Z., Mao, J. T., Wang, M. H., and Liu, X. Y.: An intensive  
712 study of aerosol optical properties in Beijing urban area, *Atmos. Chem. Phys.*, 9, 8903–8915,  
713 doi:10.5194/acp-9-8903-2009, 2009.

714 Holben, B. N., Eck, T. F., Slutsker, I., Tanre, D., Buis, J. P., Setzer, A., Vermote, E., Reagan, J. A.,  
715 Kaufman, Y. J., Nakajima, T., Lavenu, F., Jankowiak, I., and Smirnov, A.: AERONET-a federated  
716 instrument network and data archive for aerosol characterization, *Remote Sens. Environ.*, 66, 1-16,  
717 1998.

718 Holler, R., Ito, K., Tohno, S., and Kasahara, M.: Wavelength-dependent aerosol single scattering albedo:  
719 measurements and model calculations for a coastal site near the sea of Japan during ACE-Asia, *J.*  
720 *Geophys. Res.*, 108, 8648, doi:10.1029/2002JD003250, 2003.

721 IPCC 2013: Climate Change 2013: The Physical Science Basis. Contribution of Working Group I to the  
722 Fifth Assessment Report of the Intergovernmental Panel on Climate Change, edited by: Stocker, T.  
723 F., Qin, D., Plattner, G.-K., Tignor, M., Allen, S. K., Boschung, J., Nauels, A., Xia, Y., Bex, V., and  
724 Midgley, P. M., Cambridge University Press, Cambridge, UK and New York, NY, USA, 1535 pp.,  
725 2013.

726 Jacobson, M. Z.: A physically based treatment of elemental carbon optics: implication for global direct  
727 forcing of aerosols, *Geophys. Res. Lett.*, 27, 217-220, 2000.

728 Jacobson, M. Z.: Control of fossil-fuel particulate black carbon and organic matter, possibly the most  
729 effective method of slowing global warming, *J. Geophys. Res.*, 107, 4410,  
730 doi:10.1029/2001JD001376, 2002.

731 Jiang, Z., Liu, Z., Wang, T., Schwartz, C. S., Lin, H.-C., and Jiang, F.: Probing into the impact of  
732 3DVAR assimilation of surface PM<sub>10</sub> observations over China using process analysis, *J. Geophys.*  
733 *Res. Atmos.*, 118, 6738–6749, doi:10.1002/jgrd.50495, 2013.

734 Khatri, P., Ishizaka, Y., and Takamura, T.: A study on aerosol optical properties in an urban atmosphere  
735 of Nagoya, Japan. *J. Meteorol. Soc. Jpn.*, 87 (1), 19-38, 2009.

736 Kiehl, J. T. and Briegleb, B. P.: The relative roles of sulfate aerosols and greenhouse gases in climate  
737 forcing, *Science*, 260, 311–314, 1993.

738 Kuhlmann, J., and Quaas, J.: How can aerosols affect the Asian summer monsoon? Assessment during  
739 three consecutive pre-monsoon seasons from CALIPSO satellite data, *Atmos. Chem. Phys.*, 10,  
740 4673-4688, doi:10.5194/acp-10-4673-2010, 2010.

741 Li, J., Carlson, B. E., and Lacis, A. A.: Using single-scattering albedo spectral curvature to characterize  
742 East Asian aerosol mixtures, *J. Geophys. Res. Atmos.*, 120, 2037–2052, 2015c.

743 Li, J., Wang, W.-C., Liao, H., and Chang, W. Y.: Past and future direct radiative forcing of nitrate  
744 aerosol in East Asia, *Theor. Appl. Climatol.*, 121, 445–458, 2015b.

745 Li, S., Wang, T. J., Xie, M., Han, Y., and Zhuang, B. L.: Observed aerosol optical depth and angstrom  
746 exponent in urban area of Nanjing, China, *Atmos. Environ.*, 123, 350-356,  
747 doi:10.1016/j.atmosenv.2015.02.048, 2015a.

748 Liao, H. and Seinfeld, J. H.: Global impacts of gas-phase chemistry-aerosol interactions on direct  
749 radiative forcing by anthropogenic aerosols and ozone, *J. Geophys. Res.*, 110, D18208,

750 doi:10.1029/2005JD005907, 2005.

751 Ma, X. X., Liu, H. N., Liu, J., and Zhuang, B. L.: Sensitivity of climate effects of black carbon in China  
752 to its size distributions, *Atmospheric Research*, 185, 118-130, 2017.

753 Ma, X., and Yu, F.: Effect of spectral dependent surface albedo on Saharan dust direct radiative forcing.  
754 *Geophys. Res. Lett.* 39, L09808, 2012. Madronich, S.: UV radiation in the natural and perturbed  
755 atmosphere, In: Tevini, M. (Ed.), *UV-B Radiation and Ozone Depletion, Effects on Humans,*  
756 *Animals, Plants, Microorganisms, and Materials*, Lewis Publisher, Boca Raton, pp. 17-69, 1993.

757 Markowicz, K. M., Flatau, P. J., Remiszewska, J., Witek, M., Reid, E. A., Reid, J. S., Bucholtz, Z., and  
758 Hilben, B.: Observations and modeling of the surface aerosol radiative forcing during UAE. *J.*  
759 *Atmos. Sci.* 65, 2877-2891, 2008.

760 Menon, S., Hansen, J., Nazarenko, L., and Luo, Y. F.: Climate effects of black carbon aerosols in China  
761 and India, *Science*, 297, 2250–2253, doi:10.1126/science.1075159, 2002.

762 Palancar, G.G., and Toselli, B. M.: Effects of meteorology and tropospheric aerosols on UV-B radiation:  
763 a 4-year study. *Atmos. Environ.* 18, 2749-2757, 2004.

764 Pan, L, Che, H. Z., Geng, F. H., Xia, X. A., Wang, Y. Q., Zhu, C. Z., Chen, M., Gao, W., and Guo, J. P.:  
765 Aerosol optical properties based on ground measurements over the Chinese Yangtze Delta Region,  
766 *Atmos. Environ.*, 44, 2587-2596, doi:10.1016/j.atmosenv.2010.04.013, 2010.

767 Peng, Z., Liu, Z. Q., Chen, D., and Ban, J. M: Improving PM<sub>2.5</sub> forecast over China by the joint  
768 adjustment of initial conditions and source emissions with an ensemble Kalman filter, *Atmos. Chem.*  
769 *Phys.*, 17, 4837–4855, 2017.

770 Penner, J. E., Andreae, M., Annegarn, H., Barrie, L., Feichter, J., Hegg, D., Jayaraman, A., Leaitch, R.,  
771 Murphy, D., Nganga, J., and Pitari, G.: Aerosols, their direct and indirect effects, in: *Climate*

772 Change 2001: The Scientific Basis. Contribution of Working Group I to the Third Assessment  
773 Report of the Intergovernmental Panel on Climate Change, edited by: Houghton, J. T. et al.,  
774 Cambridge University Press, Cambridge, UK and New York, NY, USA, 289–348, 2001.

775 Podgorny, I. A., and Ramanathan, V.: A modeling study of the direct effect of aerosols over the  
776 tropical Indian Ocean, *J Geophys. Res.* 106, D20, 24097–24105, 2001.

777 Qi, B., Hu, D. Y., Che, H. Z., Du, R. G., Wu, Y. F., Xia, X. A., Zha, B., Liu, J., Niu, Y. W., Wang, H.,  
778 Zhang, X. Y., and Shi, G. Y.: Seasonal variation of aerosol optical properties in an urban site of the  
779 Yangtze Delta Region of China. *Aerosol Air Qual. Res.*, 16, 2884-2896, 2016.

780 Reddy, M. S., Boucher, O., Bellouin, N., Schulz, M., Balkanski, Y., Dufresne, J. L., and Pham, M.:  
781 Estimates of global multicomponent aerosol optical depth and direct radiative perturbation in the  
782 Laboratoire de Meteorologie Dynamique general circulation model, *J. Geophys. Res.*, 110, D10S16,  
783 doi:10.1029/2004JD004757, 2005.

784 Russell, P. B., Kacenelenbogen, M., Livingston, J. M., Hasekamp, O. P., Burton, S. P., Schuster, G. L.,  
785 Johnson, M. S., Knobelspiesse, K. D., Redemann, J., Ramachandran, S., and Holben, B.: A  
786 multiparameter aerosol classification method and its application to retrievals from spaceborne  
787 polarimetry, *J. Geophys. Res.-Atmos.*, 119, 9838–9863, doi:10.1002/2013JD021411, 2014.

788 Sun, H., Pan, Z., and Liu, X.: Numerical simulation of spatial-temporal distribution of dust aerosol and  
789 its direct radiative effects on East Asian climate, *J. Geophys. Res.*, 117, D13206,  
790 doi:10.1029/2011JD017219, 2012.

791 Tao, R., Che, H. Z., Chen, Q. L., Tao, J., Wang, Y. Q., Sun, J. Y., Wang, H., and Zhang, X. X.: Study of  
792 aerosol optical properties based on ground measurements over Sichuan Basin, China, *Aerosol and*  
793 *Air Quality Research*, 14: 905–915. doi:10.4209/aaqr.2012.07.0200, 2014.

794 Wang, T. J., Zhuang, B. L., Li, S., Liu, J., Xie, M., Yin, C. Q., Zhang, Y., Yuan, C., Zhu, J. L., Ji, L. Q.,  
795 and Han, Y.: The interactions between anthropogenic aerosols and the East Asian summer monsoon  
796 using RegCCMS, *J. Geophys. Res. Atmos.*, 120, doi:10.1002/2014JD022877, 2015.

797 Wang, Y., Che, H. Z., Ma, J. Z., Wang, Q., Shi, G. Y., Chen, H. B., Goloub, P., and Hao, X. J.: Aerosol  
798 radiative forcing under clear, hazy, foggy, and dusty weather conditions over Beijing, China,  
799 *Geophys. Res. Lett.*, 36, L06804, doi:10.1029/2009GL037181, 2009.

800 Weingartner, E., Saathoff, H., Schnaiter, M., Streit, N., Bitnar, B., and Baltensperger, U.: Absorption of  
801 light by soot particles: determination of the absorption coefficient by means of aethalometers, *J.*  
802 *Aerosol Sci.*, 34, 1445–1463, doi:10.1016/S0021-8502(03)00359-8, 2003.

803 Wu, Y. F., Zhang, R. J., Pu, Y. F., Zhang, L. M., Ho, K. F., and Fu, C. B.: Aerosol optical properties  
804 observed at a semi-arid rural site in northeastern China, *Aerosol Air Qual. Res.*, 12, 503–514, 2012.

805 Xia, X. A., Li, Z. Q., Holben, B., Wang, P., Eck, T., Chen, H. B., Cribb, M., and Zhao, Y. X.: Aerosol  
806 optical properties and radiative effects in the Yangtze Delta region of China, *J. Geophys. Res.*, 112,  
807 D22S12, doi:10.1029/2007JD008859, 2007.

808 Xia, X., Che, H., Zhu, J., Chen, H., Cong, Z., Deng, X., Fan, X., Fu, Y., Goloub, P., Jiang, H., Liu, Q.,  
809 Mai, B., Wang, P., Wu, Y., Zhang, J., Zhang, R., and Zhang, X.: Ground-based remote sensing of  
810 aerosol climatology in China: aerosol optical properties, direct radiative effect and its  
811 parameterization, *Atmos. Environ.*, 214, 243-251, doi:10.1016/j.atmosenv.2015.06.071, 2016.

812 Xu, J., Bergin, M. H., Greenwald, R., Schauer, J. J., Shafer, M. M., Jaffrezo, J. L., and Aymoz, G.:  
813 Aerosol chemical, physical, and radiative characteristics near a desert source region of Northwest  
814 China during ACE-Asia, *J. Geophys. Res.*, 109, D19S03, doi:10.1029/2003JD004239, 2004.

815 Xu, J., Bergin, M. H., Yu, X., Liu, G., Zhao, J., Carrico, C. M., and Baumann, K.: Measurement of

816 aerosol chemical, physical and radiative properties in the Yangtze delta region of China, *Atmos.*  
817 *Environ.*, 36, 161–173, 2002.

818 Xu, J., Tao, J., Zhang, R., Cheng, T., Leng, C., Chen, J., Huang, G., Li, X., and Zhu, Z.: Measurements  
819 of surface aerosol optical properties in winter of Shanghai, *Atmos. Res.*, 109-110, 25–35, 2012.

820 Xu, X.: Retrieval of aerosol microphysical properties from AERONET photolarimetric measurements.  
821 PhD diss., Department of Earth and Atmospheric Sciences, University of Nebraska-Lincoln, 2015.

822 Yan, P., Tang, J., Huang, J., Mao, J. T., Zhou, X.J., Liu, Q., Wang, Z. F., and Zhou, H. G.: The  
823 measurement of aerosol optical properties at a rural site in Northern China, *Atmos. Chem. Phys.*, 8,  
824 2229–2242, doi:10.5194/acp-8-2229-2008, 2008.

825 Yu, J., Che, H. Z., Chen, Q. L., Xia, X. A., Zhao, H. J., Wang, H., Wang, Y. Q., Zhang, X. X., and Shi,  
826 G. Y.: Investigation of aerosol optical depth (AOD) and Ångström exponent over the desert region  
827 of northwestern China based on measurements from the China Aerosol Remote Sensing Network  
828 (CARSNET), *Aerosol Air Qual. Res.*, 15, 2024-2036, doi:10.4209/aaqr.2014.12.0326, 2015.

829 Yu, X. N., Ma, J., Kumar, K. R., Zhu, B., An, J. L., He, J. Q., and Li, M.: Measurement and analysis of  
830 surface aerosol optical properties over urban Nanjing in the Chinese Yangtze River Delta, *Sci. Total*  
831 *Environ.*, 542, 277-291, 2016.

832 Yu, X. N., Zhu, B., Yin, Y., Fan, S. X., and Chen, A. J.: Seasonal variation of columnar aerosol optical  
833 properties in Yangtze River Delta in China, *Adv. Atmos. Sci.*, 28(6), 1326-1335,  
834 doi:10.1007/s00376-011-0158-9, 2011.

835 Zhang, L., Sun, J. Y., Shen, X. J., Zhang, Y. M., Che, H., Ma, L. Q., Zhang, Y. W., Zhang, X. Y., and  
836 Ogren, J. A.: Observations of relative humidity effects on aerosol light scattering in the Yangtze  
837 River Delta of China, *Atmos. Chem. Phys.*, 15, 8439–8454, 2015.

838 Zhang, Q., Streets, D. G., Carmichael, G. R., He, K. B., Huo, H., Kannari, A., Klimont, Z., Park, I. S.,  
839 Reddy, S., Fu, J. S., Chen, D., Duan, L., Lei, Y., Wang, L. T., and Yao, Z. L.: Asian emissions in  
840 2006 for the NASA INTEX-B mission, *Atmos. Chem. Phys.*, 9, 5131–5153,  
841 doi:10.5194/acp-9-5131-2009, 2009.

842 Zhang, W., Hu, B., Chen, C. H., Du, P., Zhang, L., and Feng, G. H.: Scattering properties of  
843 atmospheric aerosols over Lanzhou City and applications using an integrating nephelometer, *Adv.*  
844 *Atmos. Sci.*, 21(6), 848–856, 2004.

845 Zhang, X. Y., Wang, Y. Q., Niu, T., Zhang, X. C., Gong, S. L., Zhang, Y. M., and Sun, J. Y.:  
846 Atmospheric aerosol compositions in China: Spatial/temporal variability, chemical signature,  
847 regional haze distribution and comparisons with global aerosols, *Atmos. Chem. Phys.*, 12, 779–799,  
848 doi:10.5194/acp-12-779-2012, 2012.

849 Zhao, H. J., Che, H. Z., Zhang, X. Y., Ma, Y. J., Wang, Y. F., Wang, X. X., Liu, C., Hou, B., and Che,  
850 X. C.: Aerosol optical properties over urban and industrial region of Northeast China by using  
851 ground-based sun-photometer Measurement, *Atmos. Environ.*, 75, 270-278.  
852 doi:10.1016/j.atmosenv.2013.04.048, 2013.

853 Zheng, Y., Che, H. Z., Zhao, T. L., Xia, X. A., Gui, K., An, L. C., Qi, B., Wang, H., Wang, Y. Q., Yu, J.,  
854 and Zhang, X. Y.: Aerosol optical properties during the World Athletics Championships and Victory  
855 Day Military Parade over Beijing in August and September 2015, *Atmosphere*, 7(3), 47;  
856 doi:10.3390/atmos7030047, 2016.

857 Zhu, J., Che, H. Z., Xia, X. A., Chen, H. B., Goloub, P., and Zhang, W. X.: Column-integrated aerosol  
858 optical and physical properties at a regional background atmosphere in North China Plain, *Atmos.*  
859 *Environ.*, 84, 54-64, doi:10.1016/j.atmosenv.2013.11.019, 2014.

860 Zhu, J., Wang, T., Talbot, R., Mao, H., Hall, C. B., Yang, X., Fu, C., Zhuang, B., Li, S., Han, Y., and  
861 Huang, X.: Characteristics of atmospheric Total Gaseous Mercury (TGM) observed in urban  
862 Nanjing, China, *Atmos. Chem. Phys.*, 12, 12103–12118, doi:10.5194/acp-12-12103-2012, 2012.

863 Zhuang, B. L., Li, S., Wang, T. J., Deng, J. J., Xie, M., Yin, C. Q., and Zhu, J. L.: Direct radiative  
864 forcing and climate effects of anthropogenic aerosols with different mixing states over China,  
865 *Atmos. Environ.*, 79, 349–361, doi:10.1016/j.atmosenv.2013.07.004, 2013a.

866 Zhuang, B. L., Liu, Q., Wang, T. J., Yin, C. Q., Li, S., Xie, M., Jiang, F., and Mao, H. T.: Investigation  
867 on semi-direct and indirect climate effects of fossil fuel black carbon aerosol over China, *Theor.*  
868 *Appl. Climatol.*, 114, 651–672, doi:10.1007/s00704-013-0862-8, 2013b.

869 Zhuang, B. L., Wang, T. J., Li, S., Liu, J., Talbot, R., Mao, H. T., Yang, X. Q., Fu, C. B., Yin, C. Q.,  
870 Zhu, J. L., Che, H. Z., and Zhang, X. Y.: Optical properties and radiative forcing of urban aerosols  
871 in Nanjing, China, *Atmos. Environ.*, 83, 43–52, 2014a.

872 Zhuang, B. L., Wang, T. J., Liu, J., Li, S., Xie, M., Han, Y., Chen, P. L., Hu, Q. D., Yang, X. Q., Fu, C.  
873 B., Zhu, J. L.: The surface aerosol optical properties in urban area of Nanjing, west Yangtze River  
874 Delta, China, *Atmos. Chem. Phys.*, 17, 1143–1160, 2017.

875 Zhuang, B. L., Wang, T. J., Liu, J., Li, S., Xie, M., Yang, X. Q., Fu, C. B., Sun, J. N., Yin, C. Q., Liao, J.  
876 B., Zhu, J. L., and Zhang, Y.: Continuous measurement of black carbon aerosol in urban Nanjing of  
877 Yangtze River Delta, China, *Atmos. Environ.*, 89, 415–424, 2014b.

878 Zhuang, B. L., Wang, T. J., Liu, J., Ma, Y., Yin, C. Q., Li, S., Xie, M., Han, Y., Zhu, J. L., Yang, X. Q.,  
879 and Fu, C. B.: Absorption coefficient of urban aerosol in Nanjing, west Yangtze River Delta, China,  
880 *Atmos. Chem. Phys.*, 15, 13633–13646, 2015.

881



882 **Figure captions:**

883 Figure 1. Monthly variations of the total (a), scattering (b), and absorbing (c) aerosol optical depths  
884 (AOD) at 550 nm, including the ratio of the AOD in fine or coarse mode to the AOD in all mode (line  
885 with triangle markers in green) in urban area of Nanjing. The 10th, 25th, median, 75th, 90th percentile  
886 values of the all mode AOD are presented as box plots. The monthly means of the all mode AODs are  
887 presented as cycle markers in gray.

888 Figure 2. Monthly variations of the total (a), scattering (b), and absorbing aerosol (c) Ångström  
889 exponents (AE) at 440/870 nm for the all, fine and coarse modes in urban area of Nanjing.

890 Figure 3. Monthly variations of the all, fine, and coarse mode aerosol single scattering albedo (SSA) at  
891 550 nm (a) and the aerosol refractive indices at 440 nm (b) in urban area of Nanjing.

892 Figure 4. Frequency distributions of the size dependent AODs at 550 nm (a), AEs at 440/870 nm (b),  
893 SSAs at 550 nm (c) as well as the real and imaginary parts at 440 nm (c) in urban area of Nanjing.

894 Figure 5. Comparisons between CE-318 and MODIS based AOD at 550 nm and between AE at  
895 440/870 nm for CE-318 and at 412/470 nm for MODIS in Nanjing.

896 Figure 6. Comparisons between the absorbing aerosol optical depth (AAOD) at 550 nm from CE-318  
897 and surface absorption coefficient (AAC) at 520 nm from AE-31 (a) and between the column AAE at  
898 440/870 nm from CE-318 and surface AAE at 470/880 nm from AE-31 (b) in urban Nanjing.

899 Figure 7. The averaged aerosol volume size ( $\mu\text{m}^3/\mu\text{m}^2$ ) distributions in different seasons (a) and in  
900 different AOD levels in urban Nanjing.

901 Figure 8. Seasonal variations of the effective (a,  $\mu\text{m}$ ) and mean (b,  $\mu\text{m}$ ) radius of aerosols as well as the  
902 aerosol volume concentrations (c,  $\mu\text{m}^3/\text{cm}^3$ ) in the all, fine and coarse modes in urban Nanjing.

903 Figure 9. Relationships between the monthly mean values of 491 nm SSA and total Ångström exponent

904 (AE) at 491/870 nm (a), between the monthly mean values of the real refractive index at 670 nm and  
 905 AE at 491/870 nm (b), and between the monthly mean values of the SSA difference (870–491 nm) and  
 906 AE at 491/870 nm (c).

907 Figure 10. Distribution of the SSA and AAOD Curvatures in urban area of Nanjing under different  
 908 spectral SSA conditions, including monotonically decreasing, increasing SSA spectra and peaked SSA  
 909 spectra.

910 Figure 11. The aerosol vertical proportions (%) from CALIPSO, Polarization-Raman Lidar and their  
 911 average in Nanjing.

912 Figure 12. Seasonal variations of the clear sky aerosol direct radiative forcing (DRF,  $W/m^2$ ) at both  
 913 TOA (a~c) and the surface (d~f). The DRFs of the total (a, d), scattering (b, e) and absorbing (c, f)  
 914 aerosols in the all, fine and coarse modes are all investigated in urban Nanjing.

915 Figure 13. Comparisons in the absorbing aerosol DRFs ( $W/m^2$ ) between from BC SSA and from the  
 916 total aerosol DRF minus the scattering one.

917 Figure 14. Sensitivities of the TOA and the surface aerosol DRFs (day time,  $W/m^2$ ) to the different  
 918 aerosol profiles in clear conditions, for the total, scattering and absorbing aerosols.

919

920 **Tables:**

921 Table 1 Statistical summary of the columnar aerosol optical properties in urban area of Nanjing

Factors	Max	Min	Mean±SD	Median
550 nm AOD	2.3208	0.2723	0.6494±0.2852	0.5912
550 nm FAOD	2.2216	0.1468	0.5257±0.2806	0.4479
550 nm CAOD	0.9891	0.0139	0.1237±0.1076	0.0858
550 nm SAOD	2.2744	0.2443	0.6059±0.2747	0.5492
550 nm FSAOD	2.1459	0.1435	0.5014±0.2713	0.4263
550 nm CSAOD	0.8842	0.0113	0.1045±0.0957	0.0705
550 nm AAOD	0.2304	0.0020	0.0435±0.0240	0.0421
550 nm FAAOD	0.1424	0.0005	0.0244±0.0175	0.0208
550 nm CAAOD	0.1163	0.0009	0.0192±0.0145	0.0156

440/870 nm AE	1.9100	0.3085	1.2045±0.2856	1.2436
440/870 nm FAE	2.3625	0.3565	1.7083±0.2979	1.7364
440/870 nm CAE	-0.0789	-0.3805	-0.1876±0.0430	-0.1898
440/870 nm SAE	1.9916	0.2958	1.1976±0.3085	1.2386
440/870 nm FSAE	2.3653	0.3463	1.7102±0.2980	1.7368
440/870 nm CSAE	-0.1048	-0.7111	-0.3838±0.1017	-0.3864
440/870 nm AAE	3.4619	0.1483	1.3237±0.4820	1.2587
440/870 nm FAAE	4.5118	0.2912	1.7521±0.6470	1.6516
440/870 nm CAAE	3.1264	-0.0844	0.8748±0.4589	0.8209
550 nm SSA	0.9959	0.8053	0.9297±0.0335	0.9305
550 nm FSSA	0.9974	0.8388	0.9524±0.0261	0.9549
550 nm CSSA	0.9835	0.5898	0.8208±0.0754	0.8225
440 nm Real part	1.6000	1.3300	1.4423±0.0638	1.4374
440 nm Imaginary part	0.0301	0.0005	0.0084±0.0047	0.0078

- 922 AOD: Aerosol optical depth  
923 FAOD: Fine aerosol optical depth  
924 CAOD: Coarse aerosol optical depth  
925 SAOD: Scattering aerosol optical depth  
926 FSAOD: Scattering aerosol optical depth in fine mode  
927 CSAOD: Scattering aerosol optical depth in coarse mode  
928 AAOD: Absorbing aerosol optical depth  
929 FAAOD: Absorbing aerosol optical depth in fine mode  
930 CAAOD: Absorbing aerosol optical depth in coarse mode  
931 AE: Ångström exponent of total aerosols  
932 FAE: Ångström exponent of fine aerosols  
933 CAE: Ångström exponent of coarse aerosols  
934 SAE: Ångström exponent of scattering aerosols  
935 FSAE: Ångström exponent of scattering aerosols in fine mode  
936 CSAE: Ångström exponent of scattering aerosols in coarse mode  
937 AAE: Ångström exponent of absorbing aerosols  
938 FAAE: Ångström exponent of absorbing aerosols in fine mode  
939 CAAE: Ångström exponent of absorbing aerosols in coarse mode  
940 SSA: Single scattering albedo of total aerosols  
941 FSSA: Single scattering albedo of fine aerosols  
942 CSSA: Single scattering albedo of coarse aerosols

943

944 Table 2 Seasonal mean±SD of the columnar aerosol optical properties in urban area of Nanjing

Factors	MAM	JJA	SON	DJF
550 nm AOD	0.6788±0.2919	0.7508±0.3749	0.5866±0.2447	0.6560±0.2976
550 nm FAOD	0.4739±0.2613	0.6798±0.3793	0.5149±0.2462	0.5687±0.2978
550 nm CAOD	0.2048±0.1356	0.0710±0.0599	0.0717±0.0346	0.0873±0.0685
550 nm SAOD	0.6284±0.2835	0.7031±0.3728	0.5495±0.2342	0.6157±0.2829
550 nm FSAOD	0.4529±0.2552	0.6463±0.3760	0.4901±0.2366	0.5428±0.2846
550 nm CSAOD	0.1756±0.1225	0.0568±0.0497	0.0593±0.0315	0.0728±0.0601
550 nm AAOD	0.0503±0.0208	0.0477±0.0307	0.0372±0.0200	0.0403±0.0271
550 nm FAAOD	0.0211±0.0125	0.0335±0.0212	0.0248±0.0157	0.0259±0.0211
550 nm CAAOD	0.0292±0.0165	0.0142±0.0137	0.0124±0.0066	0.0144±0.0111
440/870 nm AE	0.9915±0.2385	1.2174±0.2639	1.3744±0.1907	1.3134±0.2461
440/870 nm FAE	1.7474±0.2896	1.4701±0.3075	1.7408±0.2582	1.6935±0.3019
440/870 nm CAE	-0.1998±0.0352	-0.1699±0.0471	-0.1862±0.0424	-0.1807±0.0464
440/870 nm SAE	0.9812±0.2687	1.2733±0.2950	1.3824±0.2043	1.2956±0.2697

440/870 nm SFAE	1.7555±0.2862	1.5218±0.3397	1.7492±0.2545	1.6809±0.3039
440/870 nm SCAE	-0.3752±0.0743	-0.2815±0.0678	-0.3797±0.0991	-0.4016±0.1162
440/870 nm AAE	1.1885±0.4500	0.7971±0.2657	1.3290±0.4533	1.5007±0.4520
440/870 nm FAAE	1.7352±0.6059	0.9943±0.2672	1.6715±0.5970	1.8947±0.6545
440/870 nm CAEE	0.8542±0.4665	0.3771±0.2753	0.8312±0.4479	0.9798±0.4235
550 nm SSA	0.9204±0.0313	0.9241±0.0422	0.9348±0.0331	0.9378±0.0331
550 nm FSSA	0.9527±0.0237	0.9405±0.0356	0.9518±0.0253	0.9555±0.0265
550 nm CSSA	0.8340±0.0628	0.7868±0.0953	0.8115±0.0752	0.8211±0.0810
440 nm Real part	1.4647±0.0628	1.4075±0.0609	1.4252±0.0602	1.4404±0.0582
440 nm Imaginary part	0.0084±0.0040	0.0083±0.0052	0.0080±0.0044	0.0083±0.0053

945

946 Table 3. The annual mean aerosol direct radiative forcing ( $W/m^2$ ) in urban area of Nanjing

Species	Clear sky	
	TOA	Surface
TA	-10.69±3.37	-25.54±2.83
FA	-11.17±3.09	-21.37±2.78
CA	-0.33±0.60	-6.15±2.90
SA	-16.45±2.81	-17.17±2.96
FSA	-15.08±3.18	-15.74±3.35
CSA	-2.31±1.18	-2.42±1.24
AA	5.76±1.27	-8.38±1.56
FAA	3.91±0.95	-5.63±1.16
CAA	1.99±1.07	-3.73±1.71

947

TA: Total aerosols

948

FA: Fine aerosols

949

CA: Coarse aerosols

950

SA: All scattering aerosols

951

FSA: Scattering aerosols in fine mode

952

CSA: Scattering aerosols in coarse mode

953

AA: All absorbing aerosols' forcing

954

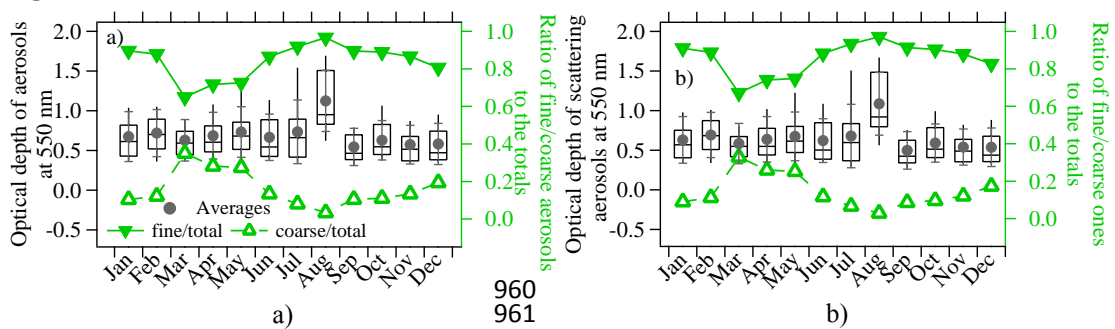
FAA: Fine absorbing aerosols' forcing

955

CAA: Coarse absorbing aerosols' forcing

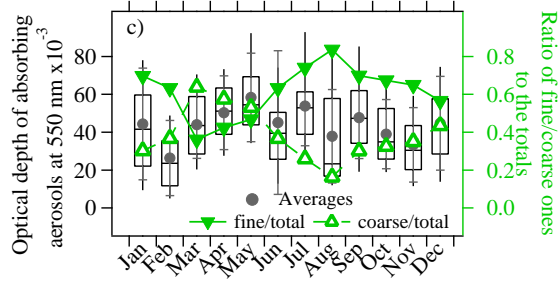
956

957 **Figures:**



958  
959

960  
961



c)  
Figure 1.

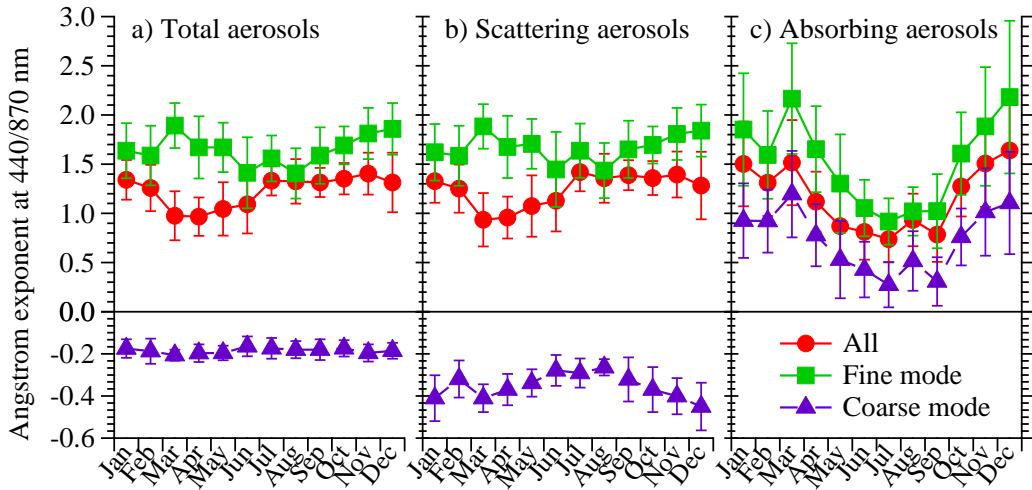


Figure 2.

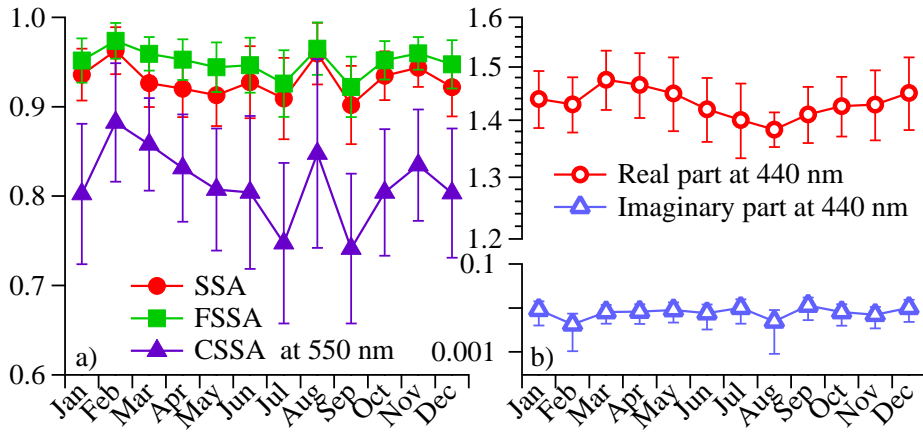
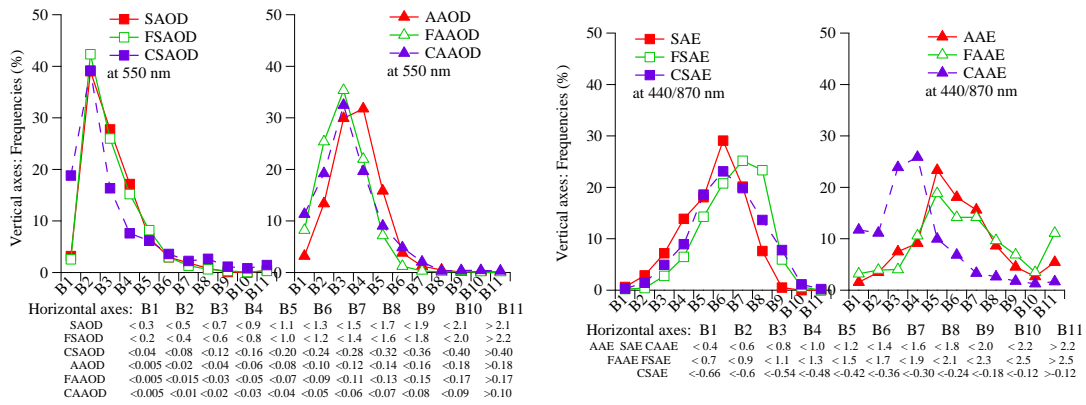


Figure 3

962  
963  
964  
965

966  
967  
968

969  
970  
971  
972



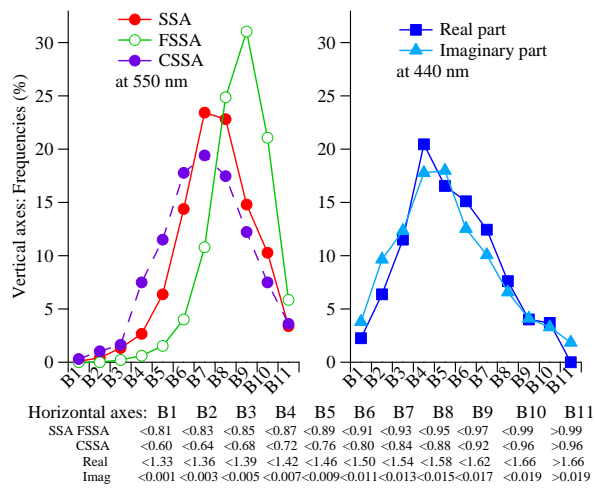
973  
974

a)

975

976

b)



977

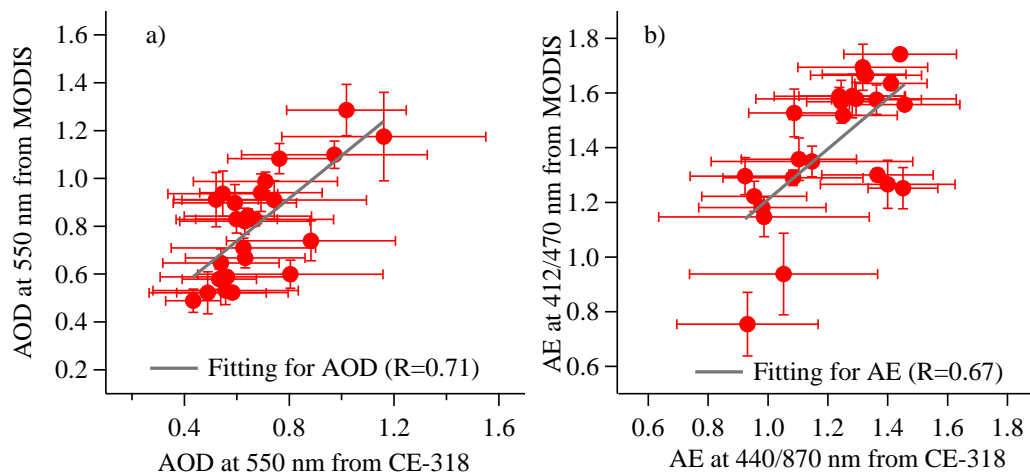
978

979

980

c)

Figure 4



981

982

983

Figure 5

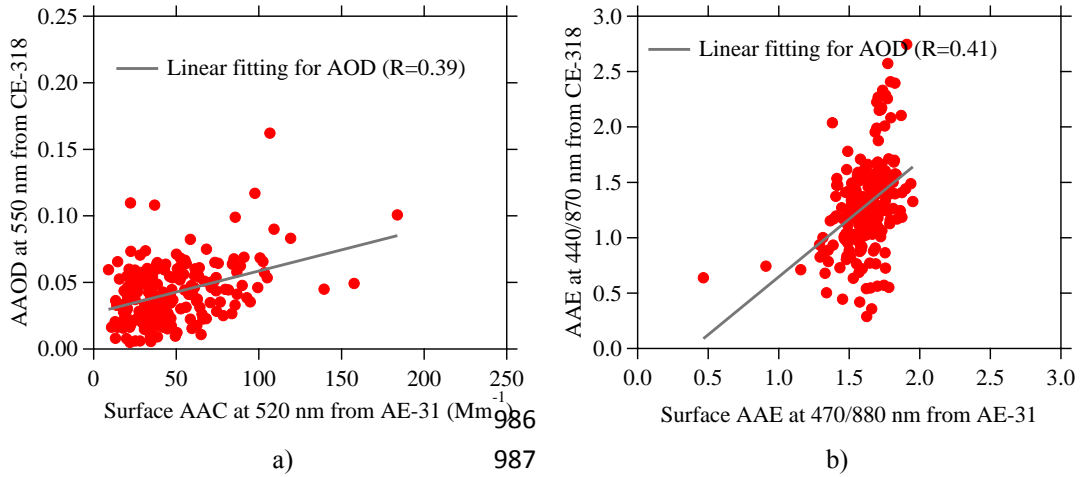


Figure 6

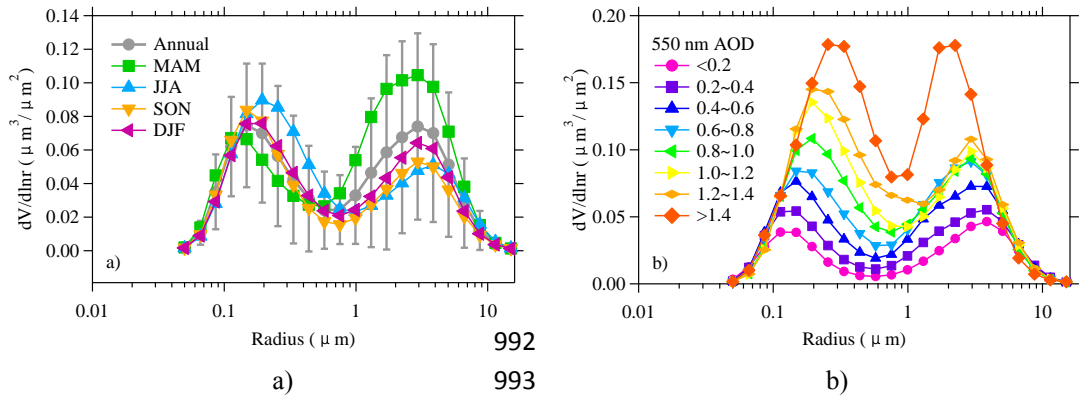


Figure 7

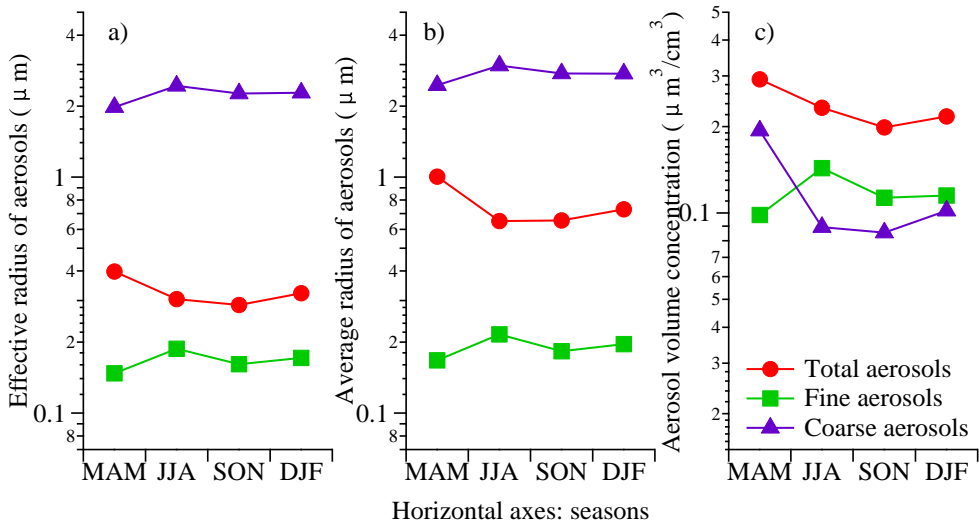
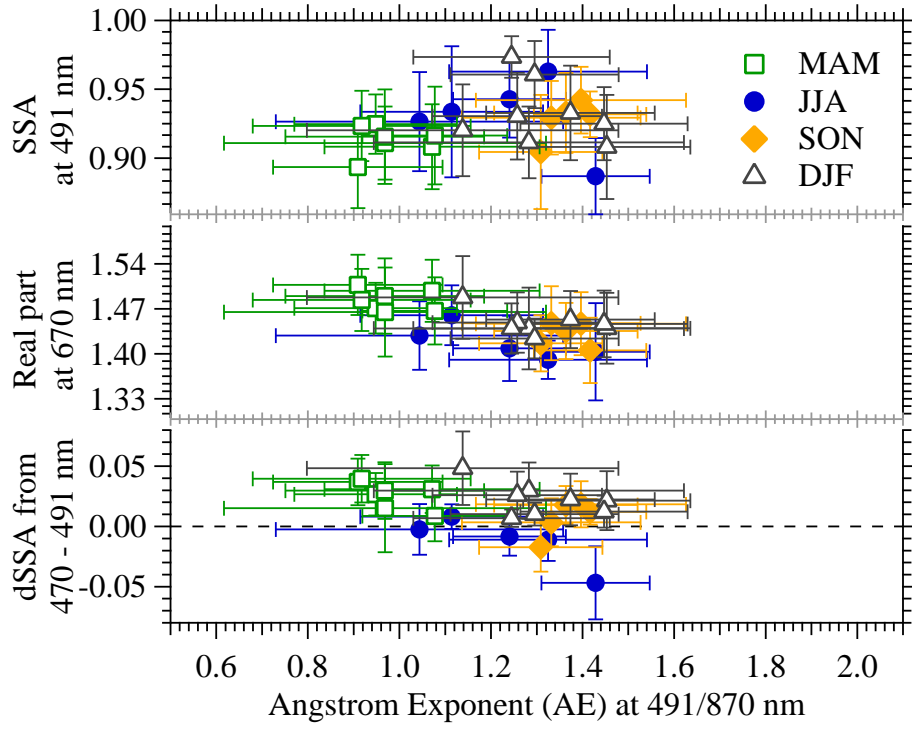
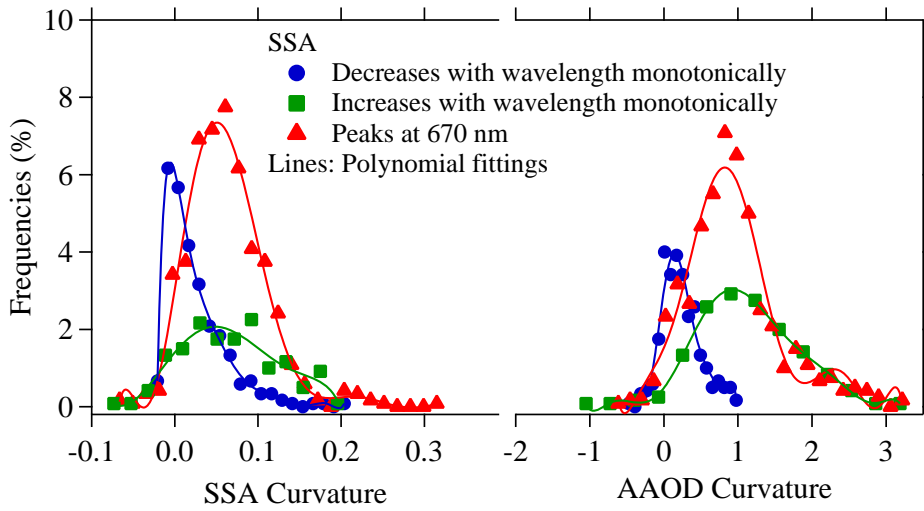


Figure 8



999  
1000  
1001

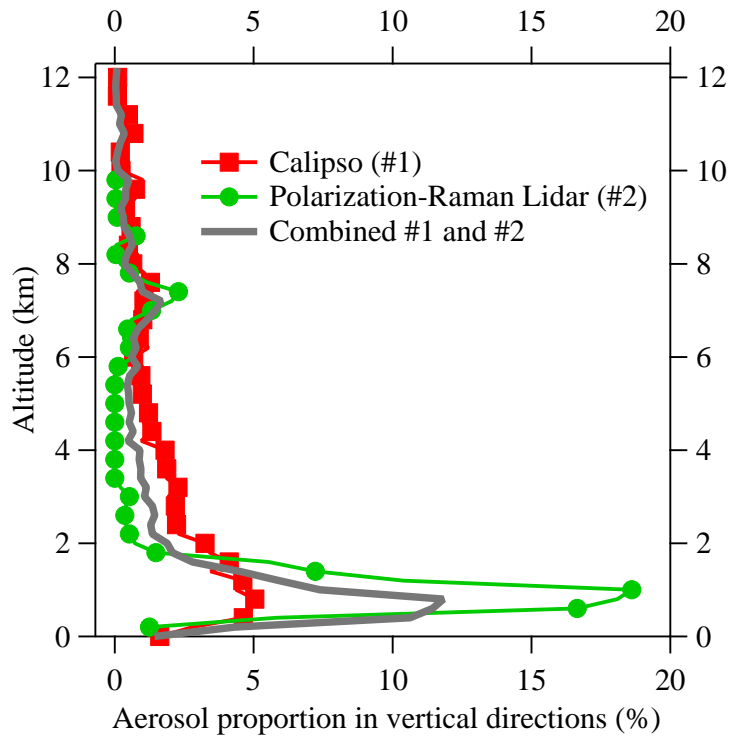
Figure 9



1002  
1003  
1004

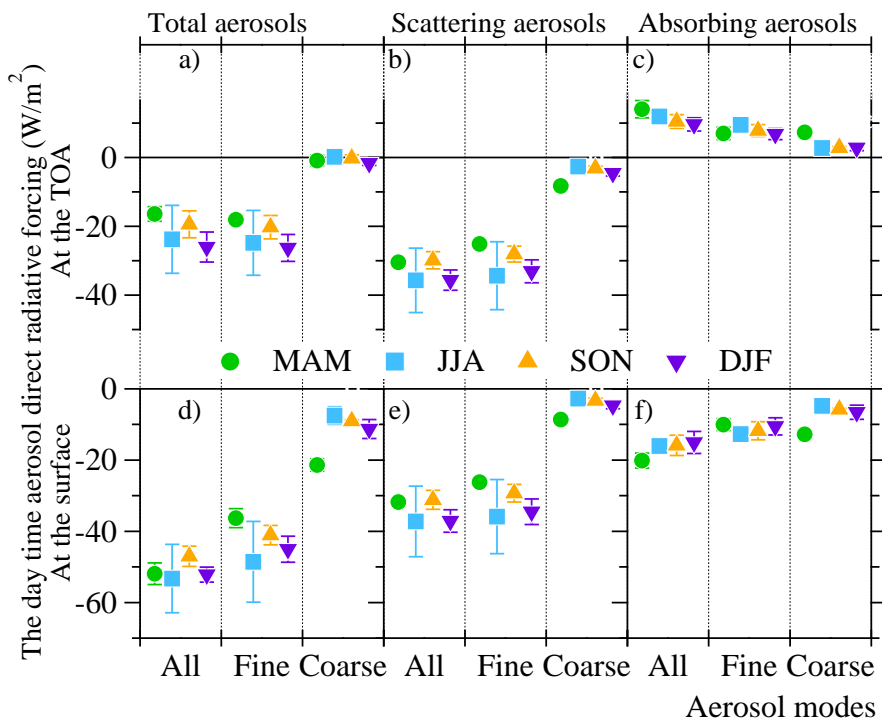
Figure 10





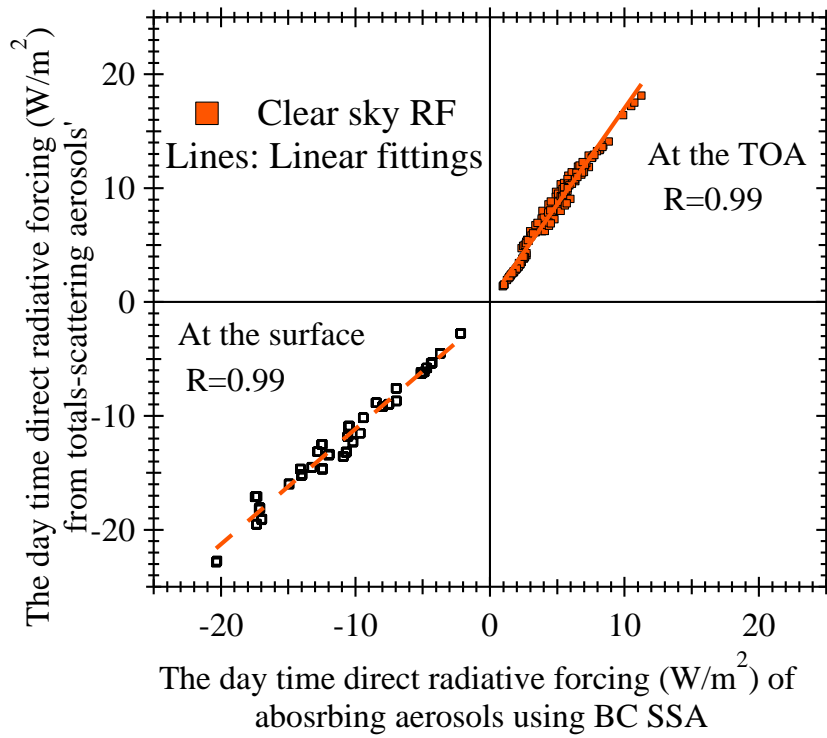
1005  
 1006  
 1007

Figure 11



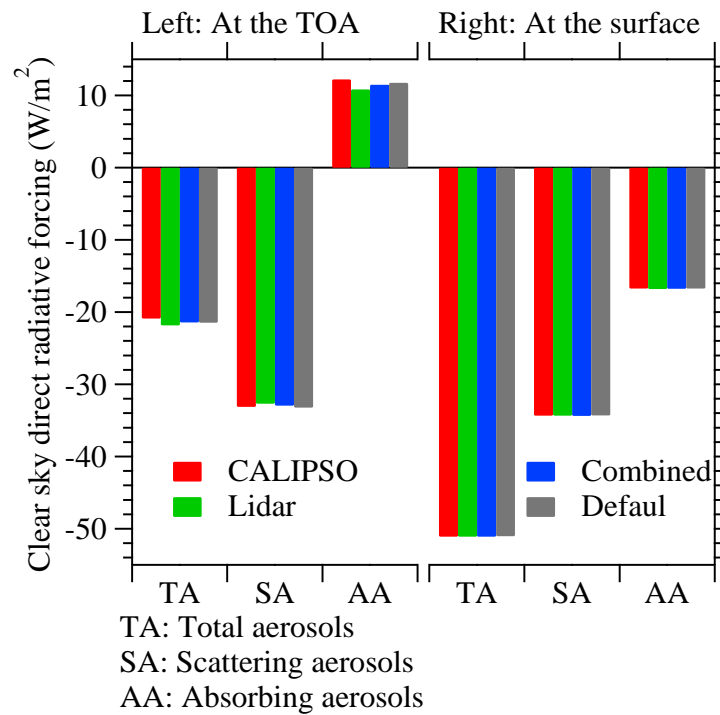
1008  
 1009  
 1010

Figure 12



1011  
 1012  
 1013

Figure 13



1014  
 1015  
 1016  
 1017

Figure 14